Mapping and Characterizing Rock Glaciers in the Arid Western Kunlun Mountains Supported by InSAR and Deep Learning

Yan Hu[1,2], Lin Liu[1,2], Lingcao Huang[3], Lin Zhao[4,5], Tonghua Wu[4], Xiaowen Wang[6,7] and Jiaxin Cai[6]

[1]Institute of Environment, Energy and Sustainability, The Chinese University of Hong Kong, Hong Kong SAR, China.

[2]Earth and Environmental Sciences Programme, Faculty of Science, The Chinese University of Hong Kong, Hong Kong SAR, China.

[3]Earth Science and Observation Center, Cooperative Institute for Research in Environmental Sciences, University of Colorado Boulder, Boulder, CO, USA.

[4]Cryosphere Research Station on the Qinghai-Tibet Plateau, State Key Laboratory of Cryospheric Science, Northwest Institute of Eco-Environment and Resources, Chinese Academy of Sciences, Lanzhou, China.

[5]School of Geographical Sciences, Nanjing University of Information Science and Technology, Nanjing, China.

[6]Faculty of Geosciences and Environmental Engineering, Southwest Jiaotong University, Chengdu, China.

[7]State-Province Joint Engineering Laboratory of Spatial Information Technology of High-Speed Rail Safety, Chengdu, China.

Corresponding author: Yan Hu (huyan@link.cuhk.edu.hk)

Key Points:

- A combined use of deep learning over optical images and InSAR automates mapping rock glaciers at the regional scale
- We compile the first rock glacier inventory in the Western Kunlun Mountains with kinematic and geomorphic information documented
- Geomorphologic characteristics of rock glaciers provide insights on the glacial and periglacial processes and interactions in the Western Kunlun Mountains

Abstract

Rock glaciers manifest the creep of mountain permafrost occurring in the past or at present. Their presence and dynamics are indicators of permafrost distribution and changes in response to climate forcing. There is a complete lack of knowledge about rock glaciers in the Western Kunlun Mountains, one of the driest mountain ranges in Asia, where extensive permafrost is rapidly warming. In this study, we first mapped and quantified the kinematics of active rock glaciers based on satellite Interferometric Synthetic Aperture Radar (InSAR) and Google Earth images. Then we trained DeepLabv3+, a deep learning network for semantic image segmentation, to automate the mapping task. The well-trained model was applied for a region-wide, extensive delineation of rock glaciers from Sentinel-2 images to map the landforms that were previously missed due to the limitations of the InSAR-based identification. Finally, we mapped 413 rock glaciers across the Western Kunlun Mountains: 290 of them were active rock glaciers mapped manually based on InSAR and 123 of them were newly identified and outlined by deep learning. The rock glaciers are categorized by their spatial connection to the upslope geomorphic units. All the rock glaciers are located at altitudes between 3,390 m and 5,540 m with an average size of 0.26 km^2 and a mean slope angle of 17°. The median and maximum surface downslope velocities of the active ones are 17±1 cm yr^{-1} and 127±6 cm yr^{-1}, respectively. Characteristics of the inventoried rock glaciers provided insights into permafrost distribution in the Western Kunlun Mountains.

Plain Language Summary

Rock glaciers are debris-ice landforms and indicators of the status of perennially frozen ground, as known as permafrost, which is warming and thawing under climate change. The Western Kunlun Mountains is among the driest mountain ranges in Asia where permafrost has been changing over the past decades and the information of rock glaciers is completely lacking. In this paper, we developed an effective workflow for mapping rock glaciers in a semi-automated manner and characterized their geomorphology and kinematics. The compiled dataset allows further investigation on rock glaciers for multiple scientific motivations such as geohazard management, water resource assessment, and permafrost change monitoring. The documented characteristics provide insights into the permafrost distribution in the arid mountains.

1 Introduction

Rock glaciers are debris-ice landforms widely distributed in areas of mountain permafrost globally (Ballantyne 2018; Jones et al. 2018). Rock glaciers have drawn a lot of research interest since their first identification at the beginning of the 20th century (Capps 1910), because they serve as visible indicators for alpine permafrost which is defined by its underground temperature and has been warming and undergoing degradation (Barsch 1996; Biskaborn et al. 2019). Inventorying rock glaciers is therefore motivated by producing baseline knowledge for addressing various scientific questions associated with permafrost, such as indicating permafrost occurrence through the rock glacier distribution, characterizing permafrost changes in the warming climate, and assessing the future hydrological significance of rock glaciers (Jones et al. 2018 and 2021). Several studies have revealed that multi-annual acceleration of rock glaciers is synchronous with the rise of air and ground temperatures (Haeberli et al. 2006; Delaloye et al. 2010; Delaloye et al. 2013; Sorg et al. 2015; Marcer et al. 2021), and their short-term velocity variations are sensitive to the pore pressure in the shear horizon which is adjusted by the precipitation and snow melt conditions (Ikeda et al. 2008; Müller et al. 2016; Wirz et al. 2016;

Cicoira et al. 2019a; Cicoira et al. 2019b; Kenner et al. 2019). Rock glacier inventories are therefore valuable datasets for setting up monitoring systems of rock glacier kinematics, which indicate permafrost changes under climate influence and can be quantified continuously and remotely. Moreover, intact rock glaciers contain ground ice and contribute to the local hydrological systems in some catchments, such as the Andes, Himalayas, and Sierra Nevada (Azócar and Brenning 2010; Millar et al. 2013; Geiger et al. 2014; Jones et al. 2018; Schaffer et al. 2019; Jones et al. 2021).

Numerous efforts have been put into inventorying rock glaciers in various mountain ranges worldwide in the past several decades, such as in Central Europe (Chueca 1992; Roer and Nyenhuis 2007; Scotti et al. 2013; Onaca et al. 2017), South America (Brenning 2005; Falaschi et al. 2014; Rangecroft et al. 2014; Villarroel et al. 2018), and North America (Ellis and Calkin 1979; Janke 2007; Millar and Westfall 2008; Liu et al. 2013). Rock glaciers are abundant in mountainous western China where a vast area of alpine permafrost is underlying and undergoing accelerated degradation in response to the warming climate (Yang et al. 2010; Cheng et al. 2019; Yang et al. 2019; Yao et al. 2019; Zhao and Sheng 2019; Ni et al. 2020; Zhao et al. 2020; IPCC 2021). However, few regional-scale inventories of rock glaciers have been compiled until recently (Schmid et al. 2015; Wang et al. 2017; Ran and Liu 2018), which hinders the application of using rock glaciers to indicate permafrost distribution. Such lack of knowledge is attributed to the following reasons: (1) rock glaciers in western China are mostly situated in remote and harsh environment where early in situ investigations are scarce and limited to case studies or small catchment-scale research (e.g., Cui 1985; Cui and Zhu 1988; Zhu et al. 1996; Harris et al. 1998); (2) mapping rock glaciers conventionally relies on manually detecting and outlining the landforms from optical images (Schmid et al. 2015), which is labor-intensive to apply to large permafrost region (e.g., Western Kunlun Mountains) following an exhaustive strategy; (3) contentious opinions of identifying rock glaciers exist due to the complexity of the landforms (Harris et al. 1998; Berthling 2011; Hu et al. 2021), which obscures the definition of rock glaciers in some previous research and makes it challenging to recognize the landforms.

To address these problems, recent research progress in compiling rock glacier inventories includes (1) integrating InSAR techniques to facilitate active rock glacier identification and kinematics quantification (e.g., Liu et al. 2013; Barboux et al. 2014; Wang et al. 2017; Cai et al. 2021; Reinosch et al. 2021; Zhang et al. 2021); (2) implementing Convolutional Neural Networks (CNN) to demonstrate the feasibility of automating rock glacier delineation (Robson et al. 2020) or to improve the consistency of existing rock glacier inventories (Erharter et al. 2022); and (3) establishing widely accepted inventorying guidelines by the international rock glacier research community (RGIK, 2022a, 2022b).

Deep learning is the computer algorithm based on neural networks that are capable of learning representations of data and determining functions to project from inputs to output (LeCun et al. 2015). It has proved powerful in semantic segmentation by using a convolutional neural network to progressively extract visual features at different levels from input images (Mottaghi et al. 2014); and it is suitable for handling difficult mapping tasks as in the case of delineating rock glaciers. Marcer (2020) first proposed a convolutional neural network to detect rock glaciers from orthoimages and suggested further development of this methodology. Robson et al. (2020) developed a new methodology to detect rock glaciers semi-automatically by advanced image processing techniques including deep learning and object-based image analysis, yet their method was not used to compile new inventories. Erharter et al. (2022) developed a

framework based on U-Net architecture to support the refinement of existing rock glacier inventories.

Here we combine the InSAR technique and a deep learning model (DeepLabv3+Xception71) to map rock glaciers across the Western Kunlun Mountains of China where knowledge of rock glaciers is completely lacking. Manual delineation of rock glaciers based on InSAR and high-resolution optical imagery in this study is guided by the baseline concepts proposed by the International Permafrost Association (IPA) Action Group on rock glaciers to ensure a standard high-quality dataset utilized to train the deep learning network, and thus, the final mapping results (RGIK, 2022a, 2022b). We adopted the deep learning method to improve the mapping efficiency by automating the identification and delineation tasks, and more importantly, to generate a more comprehensive geodatabase by overcoming the limitations of InSAR-based method, such as the coherence loss and the insensitivity to the movement perpendicular to the line-of-sight (Cai et al., 2021).

This study aims to develop an automated approach to map rock glaciers on a regional scale in western China, i.e., the Western Kunlun Mountains. By producing the first automatically mapped inventory at the mountain-range scale, we demonstrate the effectiveness of using a deep-learning-based method to delineate rock glaciers in a consistent manner across the vast study area. We provide essential attributes to the mapped landforms according to the inventorying guidelines. We also conduct statistical analyses to summarize the spatial distribution and geomorphologic characteristics of the mapped rock glaciers. The compiled inventory will provide baseline knowledge for conducting long-term studies of rock glaciers and permafrost in a changing climate.

2 Study area

The Western Kunlun Mountains is usually considered as part of the Eastern Pamir in previous research (e.g., Bolch et al. 2019a). It is situated in the northwest of Tibetan Plateau, extending ~800 km from the eastern margin of Pamir Plateau to the Keriya Pass of Kunlun Mountains, with a total study area of ~124,000 km^2 (74–81.5°E, 35–39.5°N) (Figure 1). The elevation of the study region ranges between 3,000 m and 7,500 m.

Across the vast study area, a cold desert climate (Köppen climate classification BWk) is dominant (Peel et al. 2007). Climatic conditions of the western part are revealed by the record of the nearest meteorological station in Tashikurgan (75.23°E, 37.77°N; 3090 m a.s.l.) during 1957–2017: the mean annual air temperature (MAAT) and mean annual accumulated precipitation are 4.2°C and 51 mm, respectively (data source: China Meteorological Administration, http://data.cma.cn/). The study area has been warming at a rate of ~0.033°C/yr during the past six decades (Figure S1), similar to the average warming rate (0.031°C/yr) across the entire plateau (Zhang et al. 2020). In the eastern part, the MAAT is -6 °C and the annual precipitation is 103.3 mm, as reported by the Tianshuihai meteorological station (79.55°E, 35.36°N; 4844 m a.s.l) from 2015 to 2018 (Zhao et al. 2021).

The easternmost part of the study region is overlapped with the Western Kunlun permafrost survey area (78.8–81.4°E, 34.5–36.0°N; 4,200–6,100 m a.s.l.) established by the Cryosphere Research Station (CRS) on the Qinghai-Tibet Plateau, Chinese Academy of Sciences, where in situ observations are available to represent the state of permafrost in the Western Kunlun Mountains. Ice-rich permafrost is widely distributed in the survey area (Zhao

and Sheng, 2019). The mean annual ground temperature (MAGT) is higher than -2.7°C as revealed by borehole measurements and permafrost was warming at an average rate of 0.11°C/decade from 2010 to 2017 (Cheng et al. 2019; Zhao and Sheng, 2019). The lowest altitudinal limit of permafrost occurrence is between 4,650 m and 4,800 m depending on different slope aspects according to previous field surveys focusing on a subregion of the Western Kunlun Mountains (Li et al. 2012).

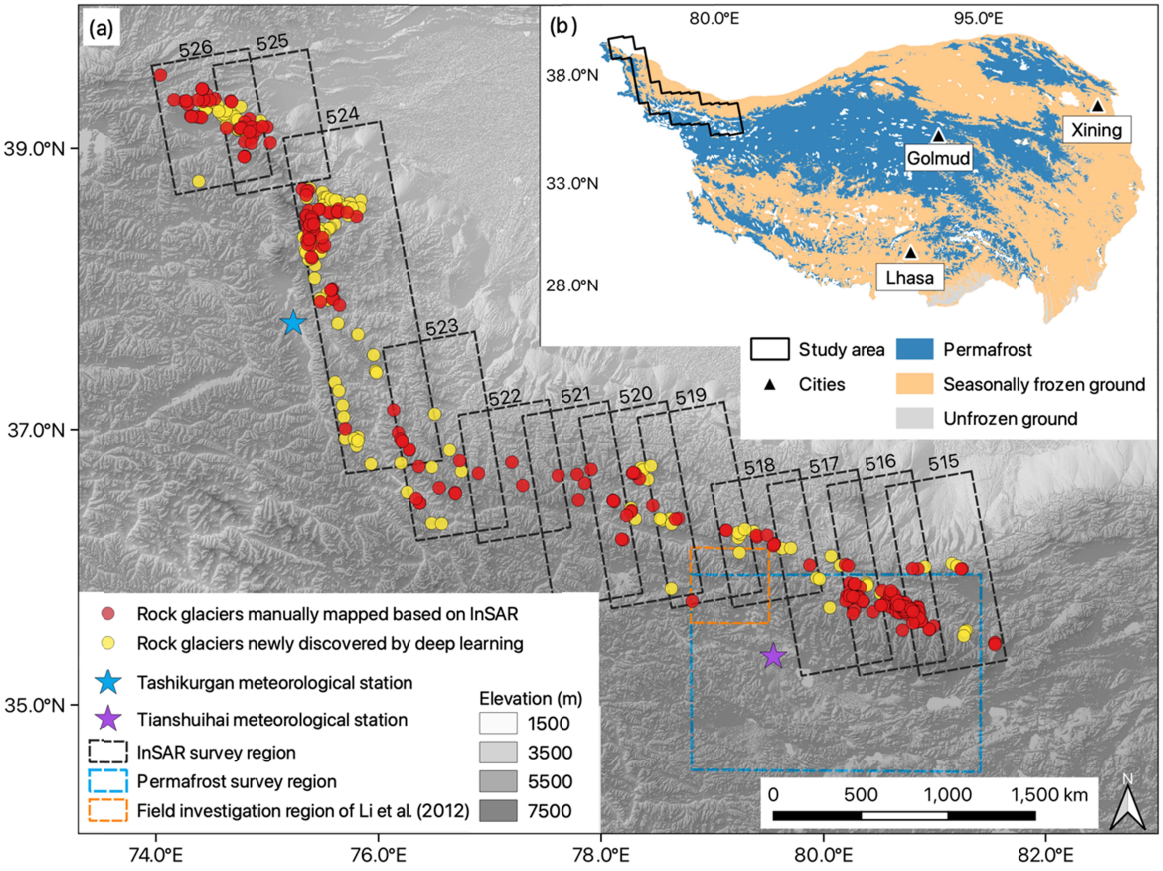

Figure 1. (a) Distribution of the mapped rock glaciers in the Western Kunlun Mountains. The red dots are manually mapped rock glaciers (290 in total), and the yellow dots represent newly identified rock glaciers by our deep learning method but were missed in the InSAR-based sub-dataset (123 in total). The background is a topographical map showing the ground coverage of ALOS-1 PALSAR data used in this study (dashed black box), with the path number of each ground track labelled aside. The dashed blue and orange boxes show the extents of the CRS permafrost survey region (Zhao and Sheng 2019), and the previous in situ investigation area (Li et al. 2012), respectively. The blue and purple stars denote the location of the Tashikurgan and Tianshuihai meteorological stations, respectively. The topography is plotted based on the 1-arcsec SRTM DEM (spatial resolution ~30 m). (b) Permafrost distribution (Zou et al. 2017) and the location of the study area on the Qinghai-Tibet Plateau.

Table 1

List of interferograms generated from ALOS-1 PALSAR data

Path/frame	Start-end dates	Perpendicular baseline (m)
515/700	20081213–20090128	300
515/710	20081213–20090128	307
516/700	20081114–20081230	-38
516/710	20081114–20081230	-31
517/700	20070829–20071014	364
517/710	20070829–20071014	370
518/710	20080317–20080502	652
519/710	20080102–20080217	972
519/720	20080102–20080217	337
520/710	20080119–20080305	581
520/720	20080119–20080305	587
521/710	20080205–20080322	62
521/720	20080205–20080322	71
522/720	20070822–20071007	212
523/720	20070608–20070724	288
523/730	20070608–20070724	289
524/730	20080210–20080327	115
524/740	20070810–20070925	108
524/750	20080210–20080327	130
524/760	20080210–20080327	137
525/770	20070712–20070827	292
526/770	20070613–20070729	471

3 Methodology

The method we adopted consists of two parts and is detailed below. First, we mapped active rock glaciers manually from interferograms and Google Earth images. Second, we used the manually labelled images to train a deep learning network, i.e., DeepLabv3+, for mapping rock glaciers automatically from Sentinel-2 optical images.

186 ### 3.1 Manual method: mapping active rock glaciers from interferograms and Google Earth
187 images

188 In this subsection, we first describe the strategy of delineating rock glaciers. Then we
189 present the method for quantifying rock glacier kinematics by InSAR. Finally, we introduce how
190 to determine the geomorphic attributes of the mapped landforms.

191 #### 3.1.1 Manual identification and delineation of rock glaciers

192 We mapped active rock glaciers by combining two imagery sources: wrapped
193 interferograms and Google Earth images (Figure 3). The displacement maps generated by InSAR
194 allow us to easily recognize moving parts of the ground surface, meanwhile the high-resolution
195 and multi-temporal Google Earth images provide geomorphic information to distinguish rock
196 glaciers from the other active surface units, such as debris-covered glaciers, solifluction lobes,
197 and slow-moving landslides. Visual identification was conducted based on the geomorphological
198 criteria proposed by RGIK (2022a, 2022b) including the frontal and lateral margin morphology,
199 and the surface ridge-and-furrow topography as an optional indicator. As much of our study area
200 is occupied by glaciers at present (Kääb et al. 2015), one challenge is to distinguish rock glaciers
201 from debris-covered glaciers. We used the updated GAMDAM glacier inventory to help
202 recognize the surrounding glacier units (Sakai, 2019), then we referred to the indicative features
203 such as the occurrence of ice cliffs, the presence of supraglacial channels, and the flow field
204 coherence, as detailed in RGIK (2022b), for identifying the landforms as rock glaciers or debris-
205 covered glaciers. We then outlined the recognized landforms along their extended
206 geomorphological footprints, i.e., the frontal and lateral margins are included within the
207 boundaries. We followed the IPA guidelines because it provides practical and standardized
208 baseline concepts for identifying and outlining rock glaciers from remote sensing images and
209 readily applicable to producing consistent inventories over wide-extent regions.

210 #### 3.1.2 Kinematic quantification by InSAR

211 In total, twenty-two interferograms generated from ALOS-1 PALSAR images covering
212 the Western Kunlun Mountains were used for ground movement detection between 2007–2009
213 (Table 1). The SAR images are in an ascending orbit. To maintain high interferometric
214 coherence and reduce topographic error, we selected image pairs with a fixed temporal spans of
215 46 days and perpendicular baselines smaller than 1,000 m. The topographic phase were
216 estimated and removed by using a digital elevation model (DEM) produced by the Shuttle Radar
217 Topography Mission (SRTM) with a spatial resolution of ~30 m over most of the study region.
218 Multi-looking operation and adaptive Goldstein filter (8×8 pixels) were applied in the
219 interferometric processing, which was implemented by the open-source software InSAR
220 Scientific Computing Environment (ISCE) version 2.2.0 (available at https://github.com/isce-
221 framework/isce2). We then unwrapped the interferograms with the SNAPHU (Chen and Zebker
222 2002) and selected one point located at the flat and stable ground close to each rock glacier to re-
223 reference the unwrapped phases measured within the boundary of each landform. By doing so,
224 we managed to remove the long-wavelength orbital errors and the atmospheric artefacts
225 including the water vapor delay and ionospheric effects, all of which can be assumed identical
226 within the extent of a rock glacier (Hanssen 2001).

227 We determined the surface downslope velocities of rock glaciers as their kinematic
228 attributes. The surface velocities along the SAR satellite line-of-sight (LOS) direction were

derived from the unwrapped interferograms and then projected to the downslope direction of each landform (Hu et al. 2021). Associated uncertainties including the InSAR measurements and geometric parameters were quantified through error propagation (Hu et al. 2021). For each rock glacier, we calculated the velocities of all the pixels within the detected moving area(s), then we used the mean velocity of all the moving pixels to represent the overall kinematic status of the rock glacier unit, if the data fulfilled the following criteria: (1) after masking out the pixels with low coherence (< 0.3) (Wang et al. 2017), the remaining pixels account for more than 40% of the entire landform extent; (2) the relative errors of the spatial mean velocities are lower than 20%.

3.1.3 Determination of geomorphic attributes

Essential geomorphic attributes such as the elevation range, mean slope angle, and landform aspect were quantified using the SRTM DEM. Qualitative attributes including the spatial connection of the rock glacier to the upslope unit and the activity category were described and assigned to the dataset following the IPA guideline (RGIK, 2022a, 2022b). We primarily classified the mapped rock glaciers according to their spatial connection to the upslope unit because it could provide implications regarding the landform genesis. Figure 2 presents examples of rock glaciers that were classified by their upslope units into four categories. For instance, Figure 2b shows a glacier-connected rock glacier, the frontal and lateral margins of which are discernible from the Google Earth image, though the rooting zone is ambiguous. We separated the rock glacier from the upslope unit from surface features such as the occurrence of exposed ice and thermokarst ponds. As suggested by RGIK (2022b), a straight line was drawn for delimiting the upper boundary of the rock glacier when it is infeasible to discern the boundary based on geomorphological and textural characteristics with high confidence. In addition, as we used the outlines for training the deep learning model to map rock glaciers from optical images (detailed in Sect. 3.2), a conservative strategy for determining the upper boundary was adopted given the relatively low resolution of the Sentinel-2 images. Finally, we created the InSAR-based sub-dataset. The entire workflow is illustrated in Figure 3 with one example shown in Figure 4.

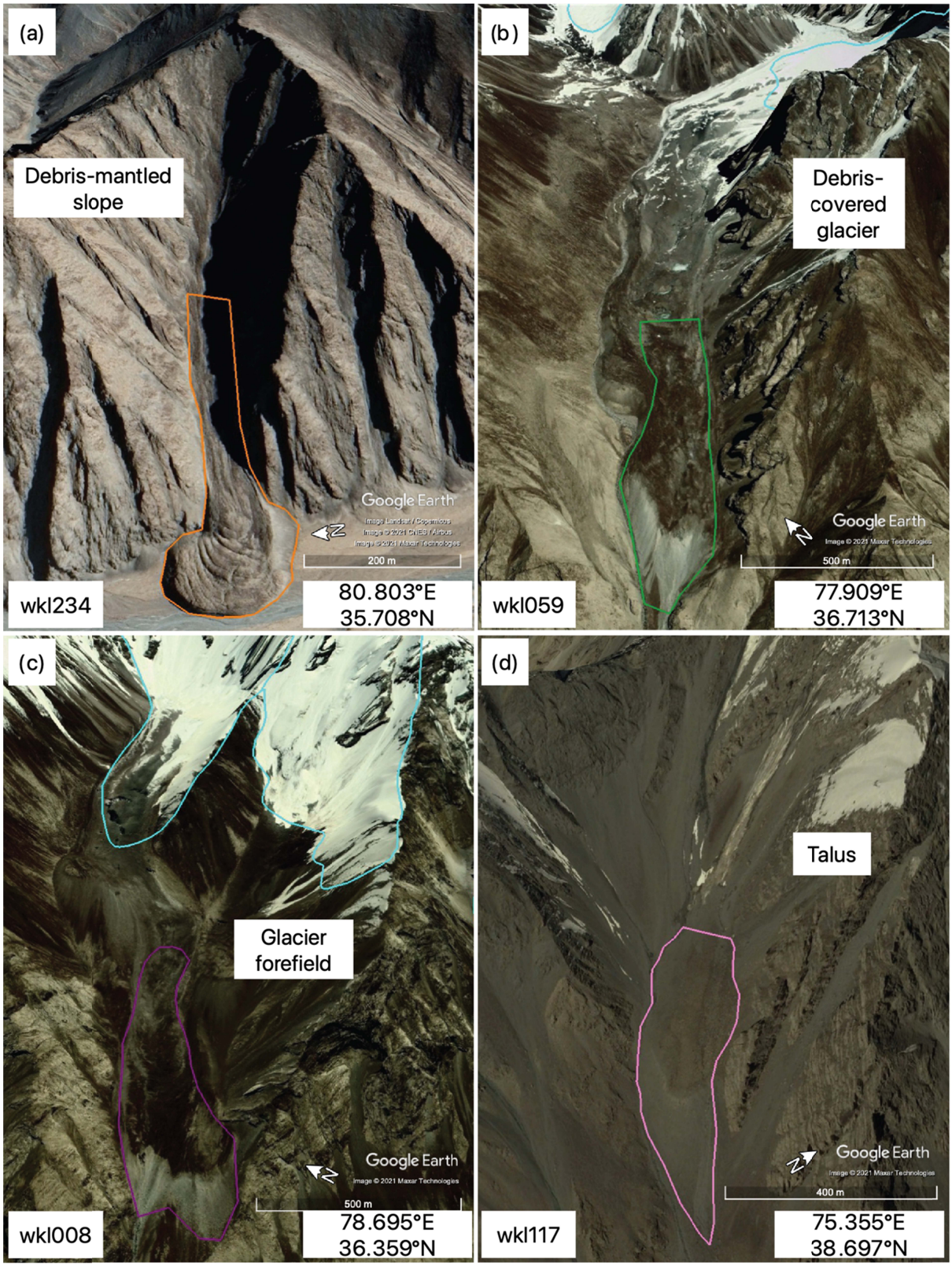
(a)
Debris-mantled slope
Google Earth
200 m
wkl234
80.803°E
35.708°N
(b)
Debris-covered glacier
Google Earth
500 m
wkl059
77.909°E
36.713°N
(c)
Glacier forefield
Google Earth
500 m
wkl008
78.695°E
36.359°N
(d)
Talus
Google Earth
400 m
wkl117
75.355°E
38.697°N
Debris-mantled slope-connected rock glaciers (DMS-RGs)
Glacier-connected rock glaciers (G-RGs)
Glacier forefield-connected rock glaciers (GF-RGs)
Talus-connected rock glaciers (T-RGs)
Glacier outlined by GLIMS

256

Figure 2. Google Earth images showing rock glaciers of four different types and their spatial connections to the upslope units. (a) shows a debris-mantled slope-connected rock glacier (DMS-RG) in orange (ID: wkl234). (b) focuses on a glacier-connected rock glacier (G-RG) in green (ID: wkl059). The cyan polygons are glaciers outlined by the GAMDAM dataset and the feature in between is recognized as a debris-covered glacier. (c) presents a glacier forefield-connected rock glacier (GF-RG) in purple (ID: wkl008). Note that the GF-RG disconnects from the upslope glacier in cyan, whereas the G-RG in (b) is in continuation of the upslope debris-covered glacier. (d) displays a talus-connected rock glacier in pink (ID: wkl117), from which the upslope talus can be observed.

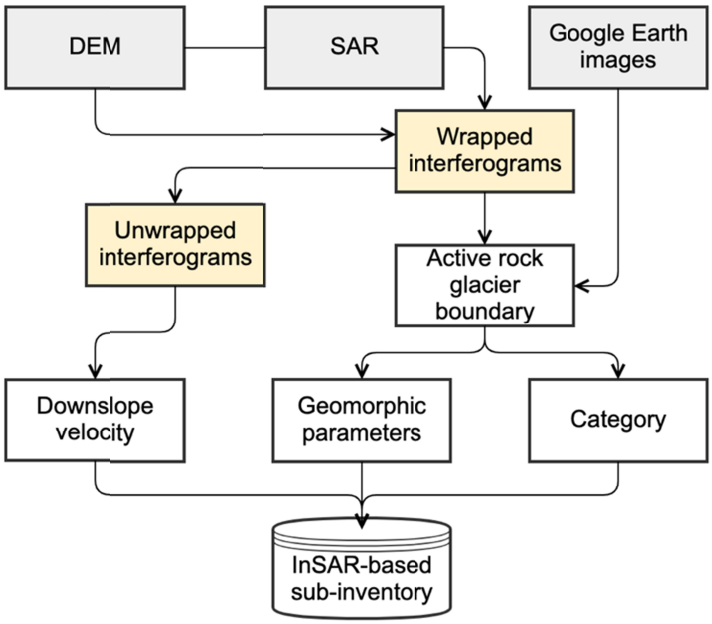

Figure 3. Diagram of the workflow to manually map active rock glaciers based on InSAR and Google Earth images.

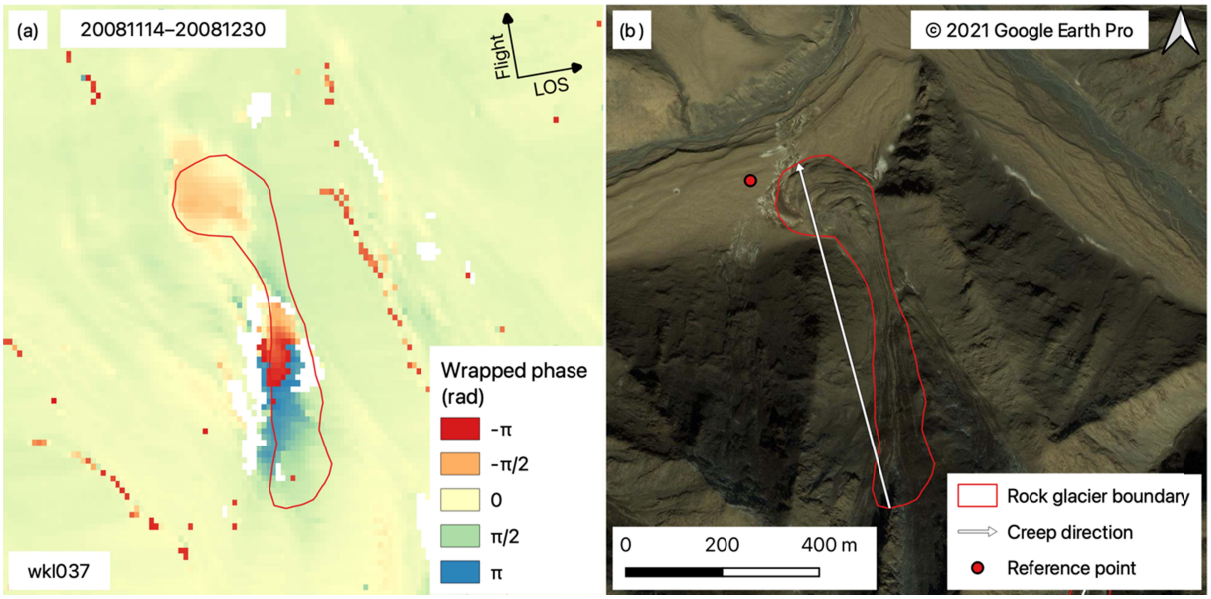

Figure 4. An example of identified active rock glacier (ID: wkl037). (a) shows the contrasting wrapped phases between the landform and surrounding background. The ALOS-1 PALSAR image pair generating the interferogram were acquired on 14/11/2008 and 30/12/2008. (b) is the corresponding Google Earth image presenting the geomorphic characteristics of the mapped active rock glacier. The white arrow indicates the direction of the movement, and the red dot marks the location of reference point used for phase correction. This rock glacier is debris-mantled slope-connected.

3.2 Automated method: mapping rock glaciers using deep learning

Among the open-source deep learning architectures designed for semantic segmentation, we adopted the DeepLabv3+ with the backbone of Xception71 (termed as DeepLabv3+Xception71 hereafter) as the framework for us to develop the automatic mapping method (Chen et al. 2018) because of its outstanding performance demonstrated in the past PASCAL VOC tests (the benchmark dataset for assessing performance of semantic segmentation models, as detailed in Everingham et al. 2015) and recent research applications to cryospheric remote sensing (Huang et al. 2020; Huang et al. 2021; Zhang et al. 2021a).

Development of the deep learning-based method for delineating rock glaciers can be divided into three major steps: (1) preparing input data, (2) training and validating deep learning network, and (3) inferring and post-processing results, as detailed below. Figure 5 illustrates the workflow and full details are provided below.

3.2.1 Preparing input data

The data preparation step aimed to produce a dataset of optical images and corresponding rock glacier label images, i.e., binary rasters that have pixel values as 0 or 1, with 1 indicating rock glaciers and 0 indicating the background, to feed into the convolutional neural network. The input optical images were cloud-free (cloud cover < 5%) Sentinel-2 Level-2A products (spatial resolution ~10 m) covering the Western Kunlun region acquired during July and August of 2019 (Table S2). We pre-processed the images by extracting the visible red, green, and blue bands and converting to 8-bit, so that the satellite images were in the same format as the training datasets used for pre-training the DeepLabv3+ network we adopted (Chen et al. 2018). To generate the label images, we used the manually identified rock glaciers in the format of ESRI Shapefiles created in the InSAR-based mapping process to label the Sentinel-2 images. We removed 118 rock glacier samples from the manually outlined rock glaciers because they are unrecognizable due to cloud cover or relatively low resolution (10 m) of the Sentinel-2 images. In addition, we delineated 145 negative polygons, which are similar-looking landforms such as debris-covered glaciers identified by GAMDAM and solifluction slopes based on our image interpretation, and environments where no rock glaciers occur, e.g., water bodies and villages. These negative polygons were used to produce negative label images which constitute the input dataset along with the positive ones. More negative samples were included during the iterative training and validating process by adding the incorrectly inferred examples to the negative training dataset for the next experiment. We extracted the positive polygons with their surrounding background (a buffer size of 1,500 m) from the optical images to provide environmental information and cropped these sub-images into image patches of sizes no larger than 480x480 pixels (Huang et al. 2018 and 2020). Finally, we split the whole dataset of input image patches by randomly selecting

90% of the data as the training set (2,007 image patches) and the remaining 10% as the validation set (223 image patches).

3.2.2 Training and validating deep learning network

Then we trained the DeepLabv3+Xception71 network with the initial hyper-parameters (e.g., learning rate, learning rate decay, batch size, number of iterations) suggested by Chen et al. (2018) and evaluated the model performance on the training and validation datasets. The model we adopted was pre-trained using the ImageNet dataset and fine-tuned during our training and validation processes. The evaluation was conducted throughout the training process by monitoring the Intersection over Union (IoU) value, which is defined as:

$$IoU=TP/(TP+FP+FN)$$

where TP (true positive), FP (false positive), and FN (false negative) are pixel-based. The mean IoU, which is calculated by averaging the IoU of each class, is commonly adopted to indicate the accuracy of semantic segmentation models (Huang et al., 2020). IoU evaluates the degree of overlap between the ground truth polygons and the predicted polygons. Our network classified each pixel of the optical images into two classes, namely the rock glacier and the background. As the amounts of pixels in the two classes are imbalanced (the rock glacier class only occupies a small portion (~10%) of the image patches), we only used the IoU value of the rock glacier class to represent the model performance. We set 0.80 as the threshold: when the IoU value of a trained model was lower than it, we increased the size and diversity of the training dataset by performing image augmentation (e.g., blurring, rotation, flip) on the positive samples and including incorrectly inferred examples to the negative samples and conducted a new experiment until obtaining a model with target IoU value on the validation dataset and regarded the deep learning network had been well trained. The IoU threshold 0.80 was selected considering the validation mIoU (79.55%) of DeepLabV3+Xception71 on the Cityscapes validation dataset, as detailed in Chen et al. (2018).

3.2.3 Inferring and post-processing results

We applied the trained model to map rock glaciers from Sentinel-2 images covering the Western Kunlun Mountains. The input data occupied ~ 0.6% of the total mapping area. To refine the inference results, we excluded the predicted polygons smaller than 30000 m^2 (~300 pixels) due to the limited spatial resolution of the Sentinel-2 images and the usual areal extent of rock glaciers (>0.01 km^2). Then we inspected each automatically delineated landform and modified the boundaries when necessary. Examples are given in Sect. 4.1. Finally, we determined the same set of landform attributes as the InSAR-based sub-dataset (Sect 3.1) and compiled the outputs produced by the two methods into one inventory.

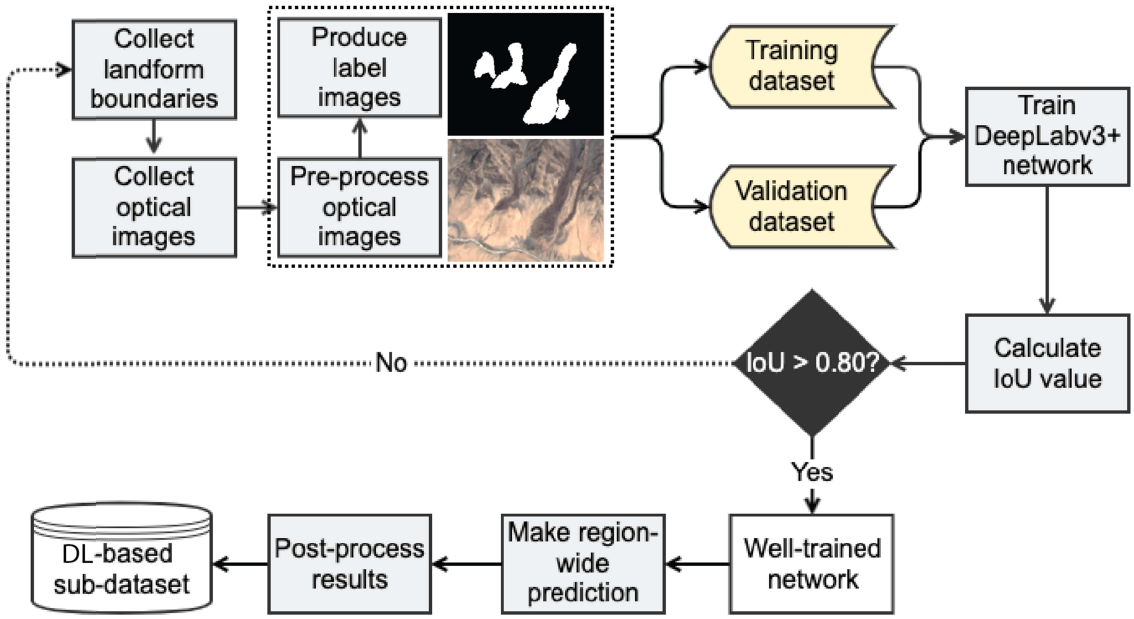

Figure 5. Diagram of the workflow to automatically map rock glaciers using DeepLabv3+ network. DL stands for deep learning.

4 Results

We produced an inventory consisting of 413 rock glaciers across the Western Kunlun Mountains: 290 of them were mapped by the conventional method based on interferograms and Google Earth images, the other 123 landforms were identified by deep learning network with supplementary modifications to the automatically delineated boundaries (Figure 1).

In this section, we first present the accuracy of the automated mapping method. Then we analyze the features of all the mapped rock glaciers from the geomorphological perspective. Finally, we summarize the kinematic characteristics of the active rock glaciers measured by InSAR.

4.1 Performance of the automated mapping approach

After iteratively training and improving the model (Sect. 3.2), we trained a model attaining a performance of IoU = 0.801 on both the training and validation datasets (Figure S2).

Over the entire Western Kunlun region, our trained model automatically identified and delineated 337 landforms as rock glaciers, among which 123 rock glaciers were newly discovered, 49 predicted polygons were false positives, the rest (165) were true positives but already present in the InSAR-based sub-dataset. Figures 6a and b present the accuracy of automated delineation by comparing the deep learning mapped rock glaciers with the manually mapped boundaries in the training and validation datasets, respectively. Specifically, Figure 6b presents an example of just passing the IoU threshold. The delineation accuracy was also acceptable for the newly discovered rock glaciers in general, as shown in Figure 6c. However, we still conducted modifications to 100 out of the 123 landforms to ensure the quality of the

mapping results after manual inspection (Figure 6d). The modification was made based on the Sentinel-2 optical images according to the geomorphic criteria presented in the IPA guideline (RGIK, 2022a, 2022b). The supplementary modifications were much less labour-intensive and time-consuming than manually identifying and delineating rock glaciers from scratch.

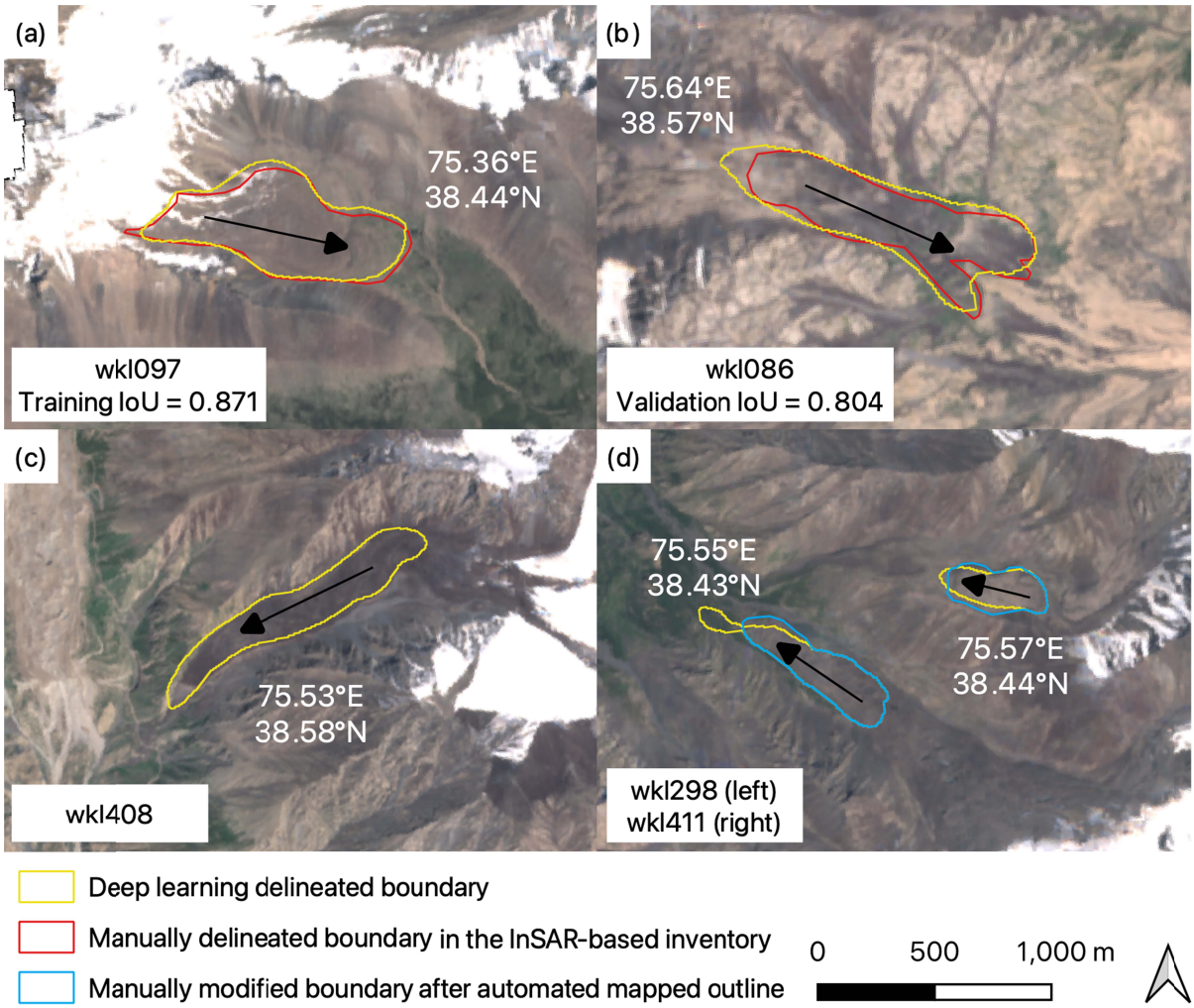

Figure 6. (a) Comparison of the deep learning mapped rock glacier boundary (in yellow) with the manually delineated polygon (in red) in the training dataset. The IoU between the two is 0.871. The black arrow indicates the flow direction. (b) Similar visual comparison between the automatically outlined boundary (in yellow) and the manually mapped one (in red) in the validation dataset, with an IoU of 0.804. (c) Example of a rock glacier newly discovered by deep learning with good delineation accuracy. (d) Examples of two automatically identified and outlined rock glaciers (in yellow) that need manual modifications (in blue). The landform IDs of these examples are labelled on the figures. The background is a Sentinel-2 image acquired on July 12th, 2019.

4.2 Geomorphic characteristics of the mapped rock glaciers

Table 2 presents the overall geomorphic information of the mapped rock glaciers. Among the 413 rock glaciers (RGs), almost half of them (202 in total) are spatially connected to glaciers

or debris-covered glaciers (G-RGs), and the debris-mantled slope-connected rock glaciers (DMS-RGs) are the second largest category, accounting for ~35% (143 in total) of the mapped landforms. There are 41 rock glaciers occurring at the glacier forefield (GF-RGs) and 27 developing at the terminus of talus (T-RGs), taking up ~10% and ~7% of the total amount, respectively.

All RGs are located at mean altitudes between 3,390 m and 5,540 m, with an average of 4,623 m. The G-RGs have a similar mean altitude of 4,546 m. Both groups (namely all RGs and the G-RGs) of landforms show a norm distribution in altitude (Figure 7a, c). The DMS-RGs generally occur at a higher altitude (Figure 7b), the average of which is up to 4,889 m, whereas the GF-RGs and T-RGs are distributed at a lower elevation band (Figure 7d, e), whose average altitudes are 4,265 m and 4,332 m, respectively.

The G-RGs are the largest with an average area of 0.40 km^2 for individual landforms, followed by GF-RGs with a mean area of 0.38 km^2. Both are much (~50%) larger than the mean area (0.26 km^2) of all RGs. The DMS-RGs are the smallest (0.05 km^2), covering ~7% of the total area occupied by all RGs in the study region. Uncertainty and variability of rock glacier boundaries can occur in inventorying practice (Brardinoni et al. 2019). In our results, as each boundary was manually examined according to the IPA guidelines, we estimated the range of uncertainty of rock glacier area within 10%. The mean surface slope of all RGs is 17º, which is similar to the mean slope (18º) of the T-RGs. The G-RGs and GF-RGs have relatively flat surfaces with mean slope angles of 14º and 15º, respectively, whereas the DMS-RGs develop a steeper average slope angle of 23º. Most (64%) of the mapped RGs occur on east-facing (0º–180º) slopes (Figure 8a) as the movement towards eastern direction is sensitive to the InSAR detection, though the AI-based sub-dataset may suffer less from this problem. Among different categories, the G-RGs and GF-RGs are more frequently located on northeastern-facing (0º–90º) slopes (Figure 8c, d), whereas the DMS-RGs and T-RGs mostly move towards southeastern directions (90º–180º) (Figure 8b, e). Finally, we briefly compared the attributes of rock glaciers between our inventory and other research focusing on the Qinghai-Tibet Plateau (Ran and Liu, 2018; Hassan et al. 2021; Reinosch et al. 2021; Zhang et al. 2022) and found similar characteristics among the existing studies (Table S3).

Table 2

Statistical summary of the geomorphic parameters of the mapped rock glaciers (All RGs), the debris-mantled slope-connected rock glaciers (DMS-RGs), the glacier-connected rock glaciers (G-RGs), the glacier forefield-connected rock glaciers (GF-RGs), and the talus-connected rock glaciers (T-RGs). Each column presents the mean values of the geomorphic parameter followed by the corresponding standard deviations in the brackets.

	Number	Mean altitude (m)	Slope (º)	Area (km^2)	Total area (km^2)
All RGs	413	4623 (431)	17 (6)	0.26 (0.28)	108.27
DMS-RGs	143	4889 (325)	23 (5)	0.05 (0.04)	7.44
G-RGs	202	4546 (412)	14 (4)	0.40 (0.29)	79.79
GF-RGs	41	4265 (430)	15 (5)	0.38 (0.32)	15.51
T-RGs	27	4332 (224)	18 (5)	0.20 (0.13)	5.53

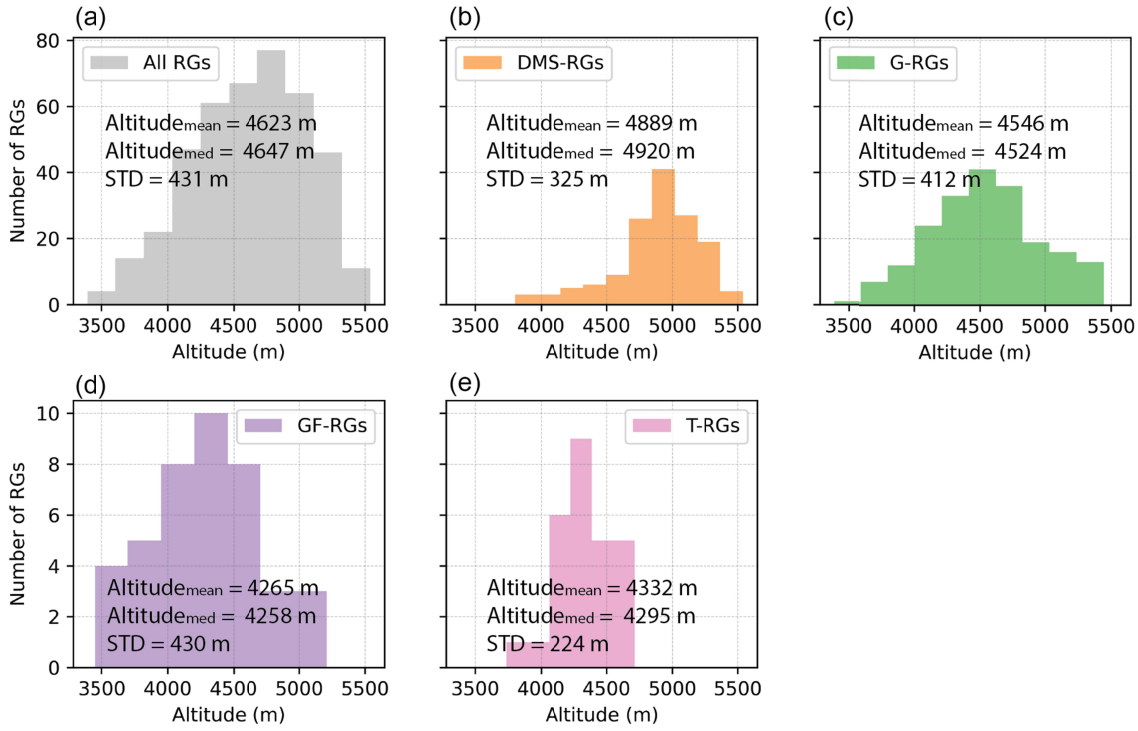

Figure 7. Histograms of the average altitudes for (a) all RGs, (b) DMS-RGs, (c) G-RGs, (d) GF-RGs, and (e) T-RGs, respectively. The altitudes are calculated from the SRTM DEM data.

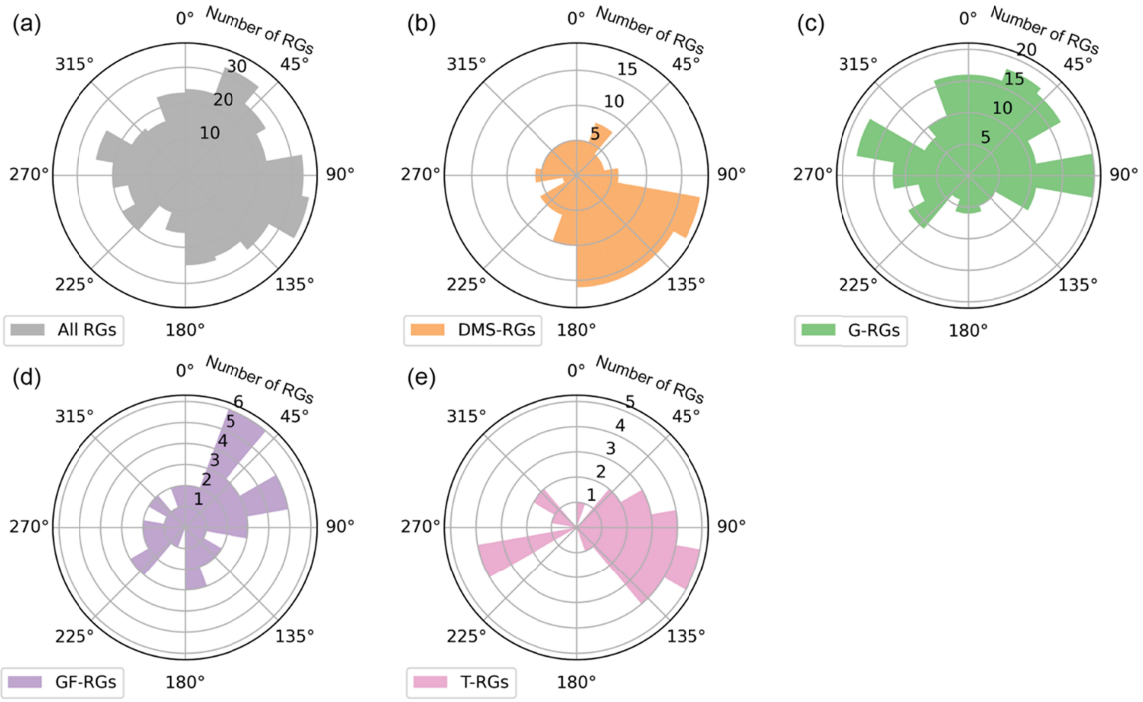

Figure 8. Histograms of the landform aspects for (a) all RGs, (b) DMS-RGs, (c) G-RGs, (d) GF-RGs, and (e) T-RGs.

4.3 Surface kinematics of the mapped active rock glaciers

Among the 290 active rock glaciers mapped based on InSAR, we obtained the surface velocities of 256 rock glaciers in total, including 115 DMS-RGs, 97 G-RGs, 21 GF-RGs, and 23 T-RGs (Figure 9). We lacked high-quality InSAR data over the rest of the mapped rock glaciers. Each velocity result was presented in the format of apparent annual velocity (unit: cm yr^{-1}) while the observation period was labelled in the dataset. Figure 10 gives examples of the velocity distributions of the four categories of rock glaciers. The spatial average velocities of the four categories are 79±6 cm yr^{-1} (Figure 10a), 44±1 cm yr^{-1} (Figure 10b), 32±1 cm yr^{-1} (Figure 10c), and 24±1 cm yr^{-1} (Figure 10d), respectively. The movement rates usually decrease towards the terminus with the highest values occurring in the upper and middle parts of the landforms.

Table 3 presents the general statistics of the documented rock glacier velocities. Most (90%) RGs move towards the downslope direction at a rate lower than 50 cm yr^{-1}, with a mean velocity of 24 cm yr^{-1}. The G-RGs and GF-RGs have faster mean velocities of 31 cm yr^{-1} and 35 cm yr^{-1}, respectively, whereas the DMS-RGs and T-RGs creep at a relatively lower rate of 17 cm yr^{-1}. The median velocities of the mapped rock glaciers are all smaller than the corresponding mean velocities, indicating the kinematic data displayed a positively skewed distribution, as shown in Figure 11. Among all the mapped rock glaciers, a DMS-RG has the largest mean velocity of 127±7 cm yr^{-1}.

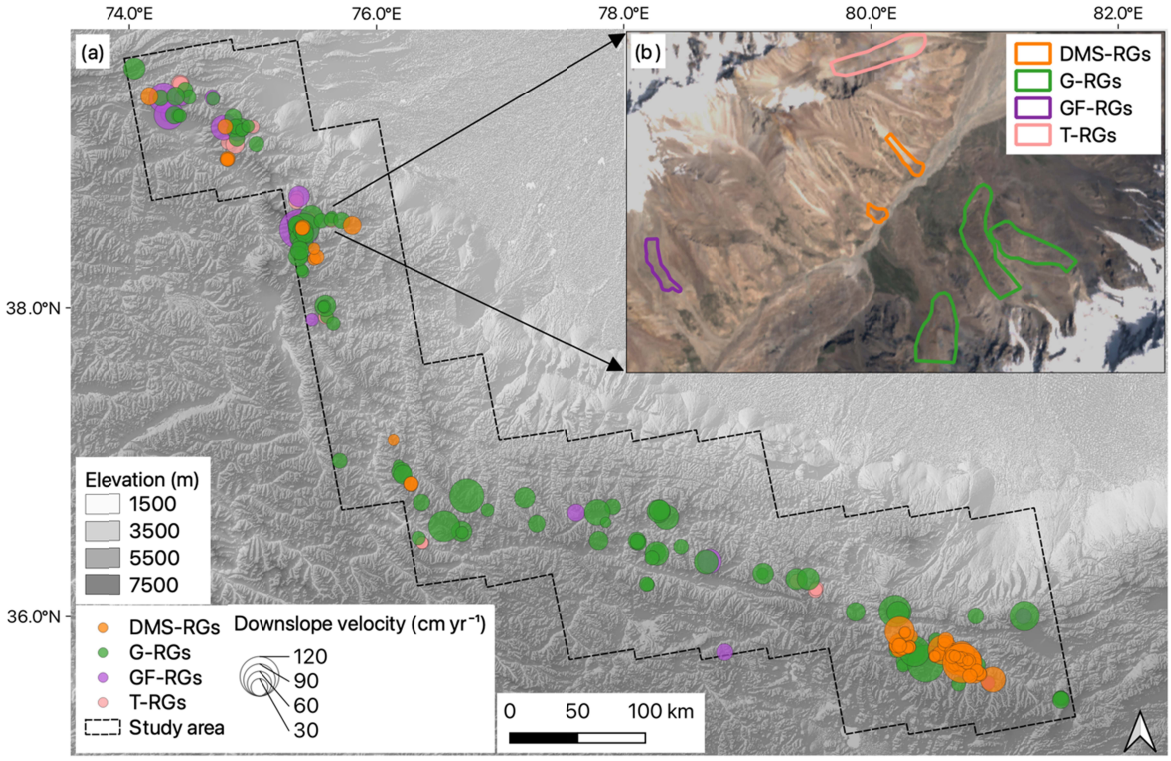

Figure 9. (a) Distribution of the mapped active rock glaciers in the study area. The four categories of rock glaciers are marked by different colours: orange for DMS-RGs, green for G-RGs, purple for GF-RGs, and pink for T-RGs. The size of the dots indicates the mean downslope velocity of each landform. The topography is mapped based on SRTM DEM. (b) shows the distribution of rock glaciers in a sub-region as indicated by the black arrows. The background is a Sentinel-2 image acquired on July 12, 2019.

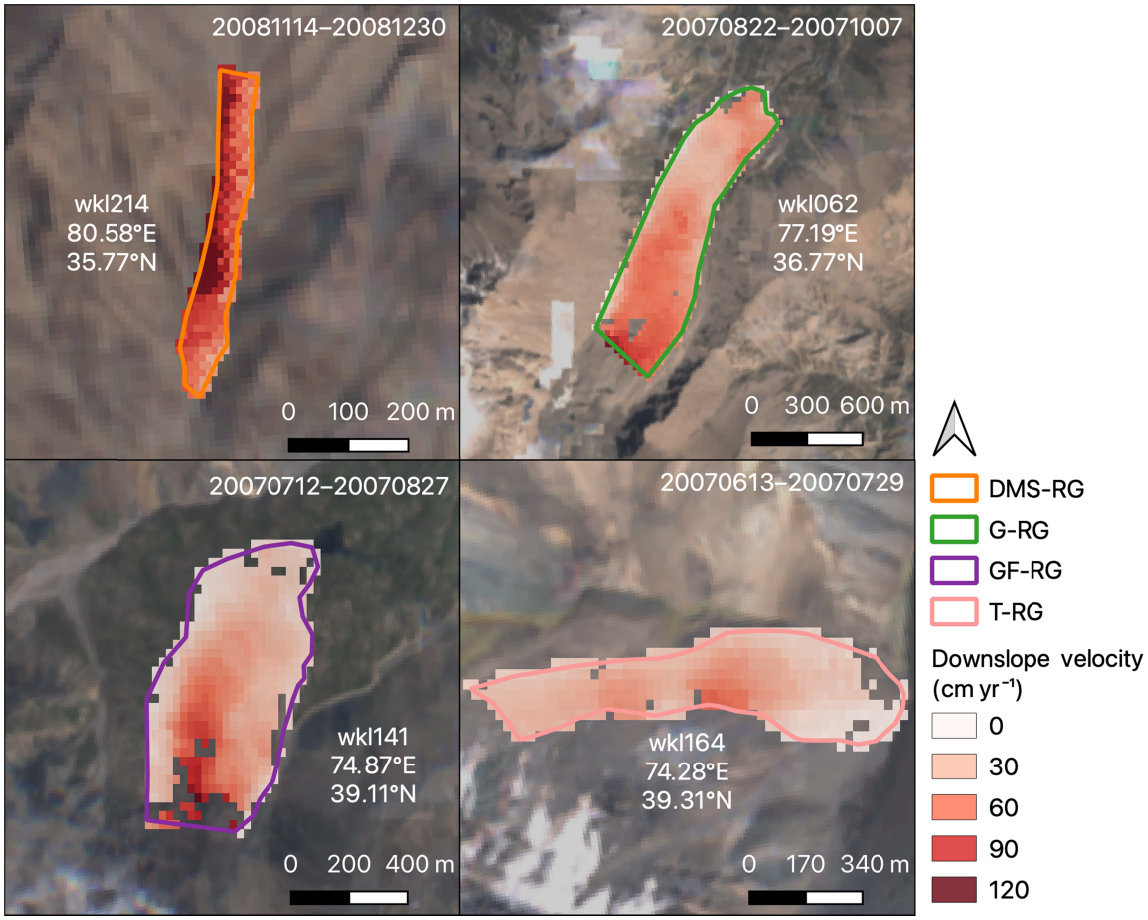

Figure 10. Velocity field maps show the downslope movement rates of rock glaciers of different categories including a DMS-RG outlined in orange (ID: wkl214), a G-RG in green (ID: wkl062) a GF-RG in purple (ID: wkl141), and a T-RG in pink (ID: wkl164). Their IDs and coordinates of central locations are labelled beside the landforms. The dates on the upper-left corners show the time spans of the velocity measurements. The background maps are Sentinel-2 images acquired in July of 2019.

Table 3

462 *Statistical summary of the kinematic features of the mapped rock glaciers. The mean velocity*
463 *column gives the mean value of the rock glacier movement rate for each category and the*
464 *standard deviations in the brackets. The median and maximum velocity columns present the*
465 *median and largest landform creep velocity in each category with their associated uncertainties,*
466 *respectively.*

	Number	Mean velocity (cm yr^{-1})	Median velocity (cm yr^{-1})	Maximum velocity (cm yr^{-1})
All RGs	256	24 (22)	17±1	127±7
DMS-RGs	115	17 (18)	12±1	127±7
G-RGs	97	31 (22)	25±1	110±1
GF-RGs	21	35 (30)	25±1	124±4
T-RGs	23	17 (8)	16±1	36±1

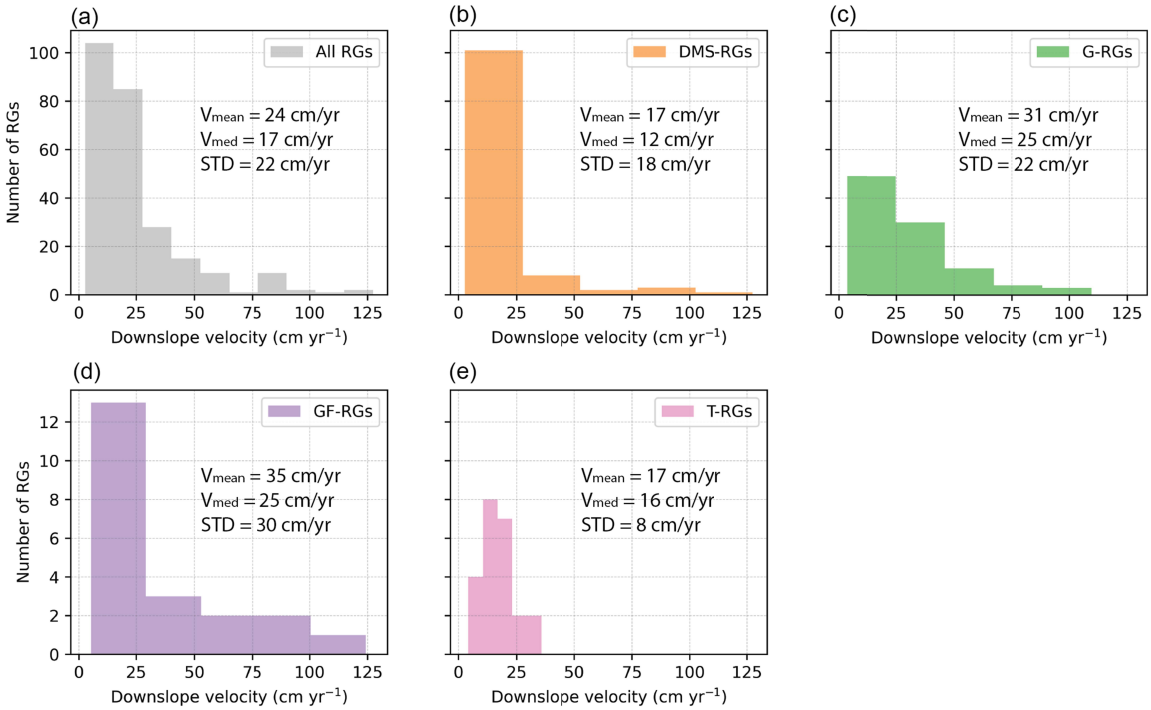

467

468 **Figure 11.** Histograms of the downslope velocities for (a) all RGs, (b) DMS-RGs, (c) G-RGs,
469 (d) GF-RGs, and (e) T-RGs, respectively.

470 **5 Discussion**

471 In this section, we first summarize the potential and limitations of using the combined
472 methodology for mapping rock glaciers (Sect. 5.1). Then we discuss the insights gained from the
473 compiled inventory about the permafrost distribution across the Western Kunlun Mountains
474 (Sect. 5.2).

5.1 Potential and limitations of the InSAR-Deep learning combined method for mapping rock glaciers

We used an InSAR-Deep learning combined approach to map rock glaciers across the Western Kunlun Mountains. The advantage of the combined methodology is twofold: the InSAR-based mapping approach provides essential information on surface kinematics and accurate manual delineation for training the deep learning model; whereas the automated method improves mapping efficiency and more importantly, overcomes the conservativeness of the former approach and expands the InSAR-based sub-dataset. More specifically, some rock glaciers cannot be detected by InSAR due to coherence loss, geometric distortions, their topographic orientations insensitive to InSAR line-of-sight measurements, or simply their inactive kinematic status (Wang et al. 2017; Robson et al. 2020). By combining with the deep learning method, we can map the landforms that had been omitted due to coherence loss in the limited number of interferograms. In addition, rock glaciers moving parallel to the satellite direction, or along a steep slope, or at a very fast or slow pace, can be mapped as well.

However, our deep learning approach has a limited level of automation: the results produced by this methodology still requires manual inspections and modifications to increase the accuracy. Among the factors controlling the deep learning performance, quality of training and validation samples is one primary factor that affects the mapping accuracy. In this study, the training and validation datasets consist of the boundaries of active rock glaciers in the InSAR-based sub-dataset overlying the Sentinel-2 optical images (Figure 5). Quality of the input images is moderate, as the Sentinel-2 images have a medium spatial resolution of ~10 m, making it challenging to characterize some rock glaciers, especially small ones (area < 30,000 m^2), from these optical images and possibly leading to inaccuracy in the output. Therefore, manual inspection is needed to build an inventory due to the false positives and a few inaccurate boundaries output by DL-based mapping method. Previous study used Sentinel-2 imagery to map rock glaciers with deep learning, but this is limited to a small region (Robson et al., 2020). Finally, the Google Earth images (2009–2020) and ALOS PALSAR data (2007–2009) we referred to while creating the InSAR-based sub-dataset are unsynchronized with the Sentinel-2 images (Jul–Aug of 2019) used for producing the training data and for predicting rock glaciers by the trained model. Accordingly, we conducted additional manual inspections while preparing the input data and recognized few differences requiring corrections to the training data because the rock glacier activity is relatively low in the study area (Sect. 4.3), yet this asynchronization may lead to errors in areas where rock glaciers have been moving fast in recent decades (Bodin et al. 2017; Marcer et al. 2021).

Furthermore, as we evaluated the effectiveness of the deep learning-based method by applying the trained model to a test area outside the original study area and the validation IoU, which reached a value of ~0.8 comparable with the previous milestone research (Chen et al., 2018), the imperfect metric we achieved (i.e., validation IoU < 1) reveals the possibility that some rock glaciers may still be missed in our inventory. We estimated the magnitude of landform underestimation by calculating an index from the validation IoU and a test experiment in a new region (methodology detailed in Text S1); yet it is challenging to provide a precise estimate given that no ground truth data is available over the study region.

In addition, our combined approach is limited to mapping intact landforms, i.e., active and transitional rock glaciers according to the updated categorization scheme of rock glacier activity proposed by RGIK (2022a, 2022b). The InSAR-based sub-inventory contains active rock

glaciers, the surface of which display coherent downslope motion as revealed by the interferograms. The transitional rock glaciers, on the other hand, show little movement over the surface, yet their geomorphologic characteristics are less distinguishable from the active landforms. Our deep learning model essentially learned the visual features of active rock glaciers through the optical images in the training dataset, and thus the model is likely to identify and delineate transitional rock glaciers as well. In contrast, relict rock glaciers usually develop distinct geomorphologic features such as subdued topography and vegetation cover, which cannot be mapped by the deep-learning model.

5.2 Insights into permafrost distribution in the Western Kunlun Mountains

By comparing the locations of rock glaciers in our inventory against three permafrost maps across the study area, we observed general consistency between the rock glacier and permafrost distribution inferred in the existing maps (Figure 12a). Moreover, we gained new insights into the different permafrost maps based on our rock glacier inventory, which can be used as an indicator of permafrost distribution (Barsch, 1996).

First, in the map generated by Obu et al. (2019), a cluster of rock glaciers (10 out of 413 inventoried landforms, ~2%) are situated in the non-permafrost zone which is consistently categorized as permafrost region in the two other maps created by Zou et al. (2017) and Ran et al. (2020) (Figure 12a–c).

Second, two rock glaciers (wkl083 and wkl085) are in a region where two out of the three maps identified as seasonally frozen ground (Figure 12d–f). However, both landforms are located close to the permafrost boundary (Zou et al., 2017) or in the transitional permafrost zone (Ran et al., 2020).

Third, besides the above examples, there are rock glaciers (12 out of 413 inventoried landforms, ~3%) occasionally situating in the area classified as seasonally frozen ground by Zou et al., (2017) but as permafrost by the other two (Obu et al., 2019; Ran et al., 2020). These rock glaciers also occur near the permafrost boundaries. Figure 12f gives an example (wkl082).

In the first case, we consider that permafrost is very likely to develop in the sub-area. In the latter two cases, however, it is challenging to determine the presence or absence of permafrost from the isolated occurrence of rock glaciers near the permafrost boundaries. As the surface debris of rock glaciers usually acts as an insulating layer (Haeberli et al., 2006), the presence of rock glaciers indicates an environment where permafrost can develop under favourable conditions. Therefore, we consider these rock glaciers to represent the occurrence of permafrost within the local extent of the landforms, but we are cautious about drawing conclusions at the regional scale.

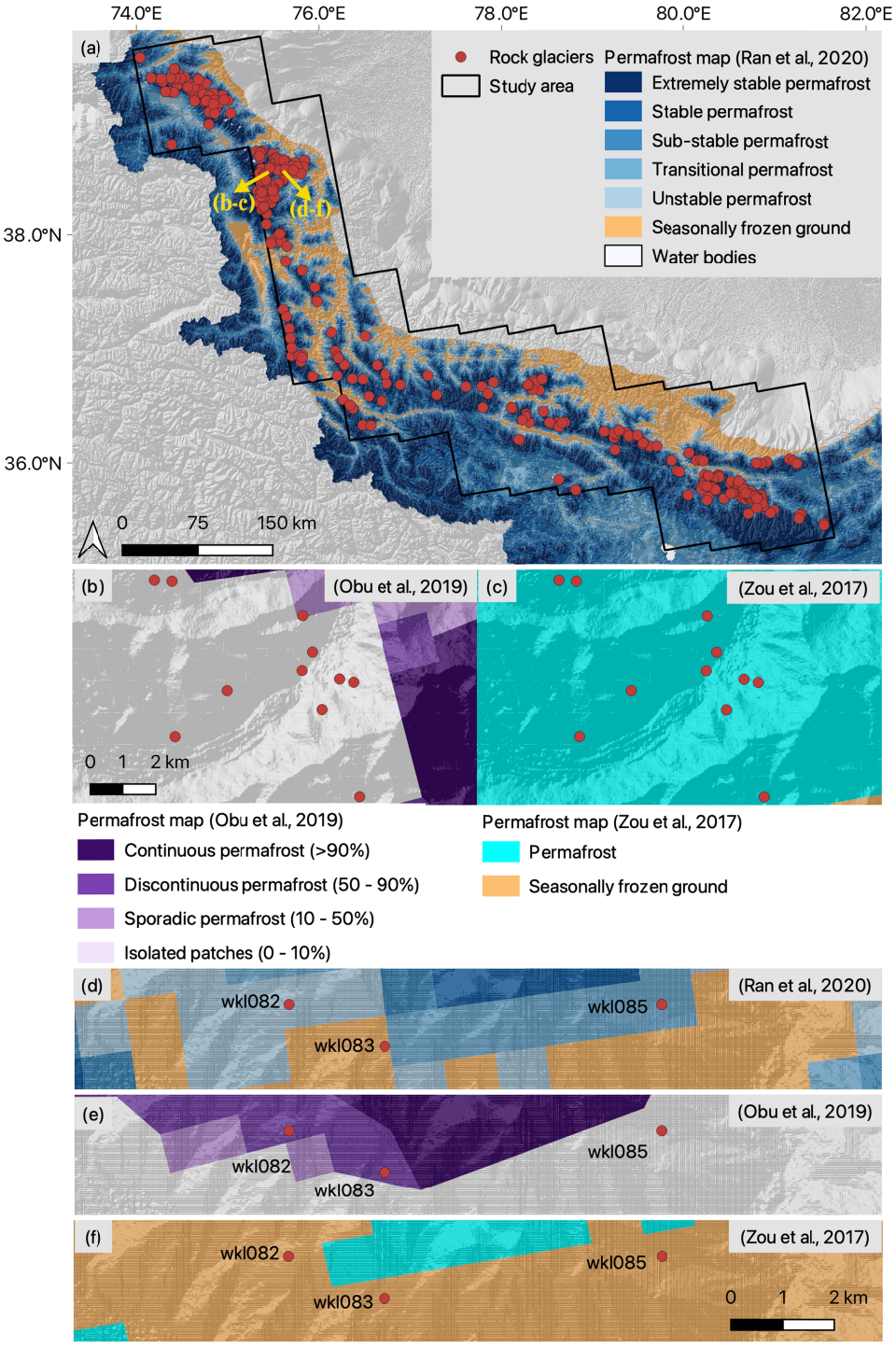

Figure 12. Comparisons between the inventoried rock glaciers and existing permafrost maps. (a) shows locations of the rock glaciers and permafrost map generated by Ran et al. (2020). (b) and (c) show the distribution of rock glaciers and permafrost over the same sub-region where different maps made contrasting predictions. (d), (e), and (f) show another sub-region where rock glaciers are situated near the permafrost boundaries identified by different maps.

6 Conclusions

We mapped rock glaciers at a regional scale and quantified their surface kinematics by combining InSAR and image semantic segmentation powered by deep learning. The deep learning method helped improve efficiency and overcome the limitations of InSAR-based mapping method. The combined method was applied to map rock glaciers across the Western Kunlun Mountains, where the extremely dry climate represents one characteristic environmental setting on the Tibetan Plateau. We draw the main conclusions as follows:

(1) The DeepLabv3+ network trained by manually labelled data based on InSAR and Google Earth images can successfully identify and delineate rock glaciers from Sentinel-2 images, attaining an IoU value of 0.801 for both training and validation datasets. The well-trained model newly mapped 123 rock glaciers to supplement the non-exhaustive InSAR-based sub-inventory of 290 active rock glaciers.

(2) There are 413 rock glaciers mapped over the study area, including 202 glacier-connected rock glaciers (G-RGs), 143 debris-mantled slope-connected rock glaciers (DMS-RGs), 41 glacier forefield-connected rock glaciers (GF-RGs), and 27 talus-connected rock glaciers (T-RGs). The mapped rock glaciers occupy a total area of ~ 108 km^2 and are located at altitudes between 3390 m and 5540 m. The average slope angle is 17° and the dominating landform aspect is towards the east.

(3) Among the mapped rock glaciers, the G-RGs and GF-RGs are larger (average areas: 0.40 km^2 and 0.38 km^2) and occur on gentler slopes (14° and 15°) predominantly facing northeast, whereas the DMS-RGs are the smallest (0.05 km^2) and occupy steep (23°) southeastern-facing slopes at the highest altitudes (4889 m). The T-RGs display a medium size (0.20 km^2) and slope angle (18°) and mostly occur on southeastern-facing slopes at lower altitudes (4332 m). The GF-RGs have the lowest average altitude (4265 m).

(4) We adopted the spatial average velocity of all pixels within the boundary of each rock glacier to represent the landform surface kinematics. In total, 256 rock glaciers have valid kinematic quantifications. Nearly 90% of the rock glaciers move slower than 50 cm yr^{-1}. The mean downslope velocity is 24 cm yr^{-1}, and the standard deviation is 22 cm yr^{-1}. The median and maximum velocities are 17±1 cm yr^{-1} and 127±6 cm yr^{-1}, respectively.

(5) Among the active rock glaciers, the G-RGs and GF-RGs move faster at mean velocities of 31 cm yr^{-1} and 35 cm yr^{-1}, respectively. The DMS-RGs and T-RGs creep at a slower average velocity of 17 cm yr^{-1}.

In summary, combining InSAR and optical imagery to manually map active rock glaciers proves to be an effective way to quantify rock glacier kinematics consistently in remote areas. The inventory produced by this work will serve as an important database for scientific investigations such as managing geohazards (e.g., Kummert and Delaloye, 2018), assessing sediment budget (e.g., Kofler et al., 2022), and monitoring permafrost changes (e.g., Haberkorn et al. 2021; Thibert and Bodin, 2022).

Several improvements can be implemented to optimize the deep learning method: (1) to increase the amount and diversity of training samples by including rock glacier boundaries from other regions; (2) to adopt higher-resolution and more cloud-free optical images for producing input dataset; and (3) to use generative adversarial network for translating optical images (for landform inference) to the domain of training data and include them during training. With the

utilization of improved deep learning techniques, it is promising to compile rock glacier inventories efficiently over a significant extent of permafrost areas, e.g., the Tibetan Plateau, which provides a baseline dataset and allows the monitoring of rock glaciers as indicators of permafrost degradation and potential water sources in a changing climate.

Acknowledgments

The authors declare that they have no known competing interest that could have appeared to influence the work presented in this paper. This work was supported by the Hong Kong Research Grants Council [grant numbers CUHK14303417, CUHK14303119, and HKPFS PF16-03859]; the National Natural Science Foundations of China [grant number 41690142 and 42071410]; the CUHK Direct Grant for Research [grant number 4053282 and 4053426]; and the CAS "Light of West China" Program.

Open Research

Data Availability Statement

The ALOS-1 PALSAR data were copyrighted and provided by the Japan Aerospace Exploration Agency through the EO-RA2 project ER2A2N081. The TanDEM-X DEM data were copyrighted and provided by the German Aerospace Centre through project DEM_GLAC1408. The Sentinel-2 (ESA) image courtesy of the U.S. Geological Survey. Figures were made with Matplotlib version 3.4.1 (Caswell et al., 2021; Hunter, 2007), available under the Matplotlib license at https://matplotlib.org/. Maps were plotted by using QGIS (QGIS Development Team, 2009), available at http://qgis.osgeo.org. SAR interferograms were generated using ISCE version 2.2.0 (ISCE, 2021), available at https://github.com/isce-framework/isce2. The rock glacier inventory produced by this work will be available on PANGAEA (https://doi.org/10.1594/PANGAEA.938686, the link will become accessible once the related paper is published). The training data will be provided by Y. Hu upon request. Codes are available on Zenodo (https://doi.org/10.5281/zenodo.7824698).

References

Azócar, G. F., & Brenning, A. (2010). Hydrological and geomorphological significance of rock glaciers in the dry Andes, Chile (27°–33°S). *Permafrost and Periglacial Processes*, *21*(1), 42–*53*. https://doi.org/10.1002/ppp.669

Ballantyne, C. K. (2018). *Periglacial geomorphology*. Oxford UK: John Wiley & Sons.

Barboux, C., Delaloye, R., & Lambiel, C. (2014). Inventorying slope movements in an Alpine environment using DInSAR. *Earth Surface Processes and Landforms*, *39*(15), 2087–2099. https://doi.org/10.1002/esp.3603

Barsch, D. (1996). *Rockglaciers: indicators for the present and former geoecology in high mountain environments* (Vol. 16). Springer Science & Business Media.

Berthling, I. (2011). Beyond confusion: Rock glaciers as cryo-conditioned landforms. Geomorphology, *131*(3–4), 98–106. https://doi.org/10.1016/j.geomorph.2011.05.002

Bertone, A., Barboux, C., Bodin, X., Bolch, T., Brardinoni, F., Caduff, R., et al. (2022). Incorporating InSAR kinematics into rock glacier inventories: insights from 11 regions worldwide. *Cryosphere*, *16*(*7*), 2769–2792. https://doi.org/*10*.5194/tc-16-2769-2022

Biskaborn, B. K., Smith, S. L., Noetzli, J., Matthes, H., Vieira, G., Streletskiy, D. A., et al. (2019). Permafrost is warming at a global scale. *Nature Communications*, *10*(1), 264. https://doi.org/10.1038/s41*467*-018-08240-4

Bodin, X., Krysiecki, J.-M., Schoeneich, P., Roux, O. L., Lorier, L., Echelard, T., et al. (2017). The 2006 Collapse of the Bérard Rock Glacier (Southern French Alps). Permafrost and Periglacial Processes, 28(1), 209–223. https://doi.org/10.1002/ppp.1887

Bolch, T., Shea, J. M., Liu, S., Azam, F. M., Gao, Y., Gruber, S., et al. (2019a). Status and change of the cryosphere in the extended Hindu Kush Himalaya region. In P. Wester, A. Mishra, A. Mukherji, & A. B. Shrestha (Eds.), *The Hindu Kush Himalaya Assessment, Mountains, Climate Change, Sustainability and People* (pp. 209–255). Cham: Springer International Publishing. https://doi.org/10.1007/978-3-319-92288-1_7

Brardinoni, F., Scotti, R., Sailer, R., & Mair, V. (2019). Evaluating sources of uncertainty and variability in rock glacier inventories. *Earth Surface Processes and Landforms*, *44*(12), 2450–2466. https://doi.org/10.1002/esp.4674

Brenning, A. (2005). Geomorphological, hydrological and climatic significance of rock glaciers in the Andes of Central Chile (*33*–35°S). Permafrost and Periglacial Processes, 16(3), *23*1–240. https://doi.org/10.1002/ppp.528

Cai, J., Wang, X., Liu, G., & Yu, B. (2021). A comparative study of active rock glaciers mapped from geomorphic-and kinematic-based approaches in daxue shan, southeast tibetan plateau. *Remote Sensing*, *13*(23), 4931. https://doi.org/*10*.3390/rs1*3*234931

Capps, S. R. (1910). Rock Glaciers in Alaska. *The Journal of Geology*, *18*(4), 359–375. https://doi.org/10.1086/62*1*746

Caswell, T. A., Droettboom, M., Lee, A., Andrade, E. S. de, Hunter, J., Hoffmann, T., et al. (2021). matplotlib/matplotlib: REL: v3.4.1 [Software]. Zenodo. https://doi.org/10.5281/zenodo.4649959

Chen, C. W., & Zebker, H. A. (2002). Phase Unwrapping for Large Sar Interferograms: Statistical Segmentation and Generalized Network Models. *IEEE Transactions on Geoscience and Remote Sensing*, *40*(8), 1709. https://doi.org/10.*11*09/tgrs.2002.802453

Chen, L.-C., Zhu, Y., Papandreou, G., Schroff, F., & Adam, H. (2018). Encoder-Decoder with Atrous Separable Convolution for Semantic Image Segmentation. *ArXiv*.

Cheng, G., Zhao, L., Li, R., Wu, X., Sheng, Y., Hu, G., et al. (2019). Characteristic, changes and impacts of permafrost on Qinghai-Tibet Plateau. *Chinese Science Bulletin*, *64*(27), 2783–2795. https://doi.org/10.1360/tb-2019-0191

Chueca, J. (1992). A statistical analysis of the spatial distribution of rock glaciers, Spanish Central Pyrenees. Permafrost and Periglacial Processes, 3(3), 261–265. https://doi.org/10.1002/ppp.3430030316

677 Cicoira, A., Beutel, J., Faillettaz, J., Gärtner-Roer, I., & Vieli, A. (2019). Resolving the influence of
678 temperature forcing through heat conduction on rock glacier dynamics: A numerical modelling approach.
679 Cryosphere, 13(3), 927–942. https://doi.org/10.5194/tc-13-927-2019

680 Cicoira, A., Beutel, J., Faillettaz, J., & Vieli, A. (2019). Water controls the seasonal rhythm of rock
681 glacier flow. *Earth and Planetary Science Letters*, *528*, 115844.
682 https://doi.org/10.1016/j.epsl.2019.115844

683 Cui, Z. (1985). Discovery of Kunlunshan-type rock glaciers and the classification of rock glaciers. *Kexue*
684 *Tongbao*, *30*(3), 365–369. https://doi.org/10.1360/sb1985-30-3-365

685 Cui, Z., & Cheng, Z. (1988). Rock glaciers in the source region of Urumqi River, middle Tian Shan,
686 China (pp. 724–727). Presented at the 5th International Conference on Permafrost.

687 Delaloye, R., Lambiel, C., & Gärtner-Roer, I. (2010). Overview of rock glacier kinematics research in the
688 Swiss Alps: Seasonal rhythm, interannual variations and trends over several decades. *Geographica*
689 *Helvetica*, *65*(2), 135–145. https://doi.org/10.5194/gh-65-135-2010

690 Delaloye, R., Morard, S., Barboux, C., Abbet, D., Gruber, V., Riedo, M., & Gachet, S. (2013). Rapidly
691 moving rock glaciers in Mattertal. Geographica Helvetica, 21–31.

692 Ellis, J. M., & Calkin, P. E. (1979). Nature and Distribution of Glaciers, Neoglacial Moraines, and Rock
693 Glaciers, East-Central Brooks Range, Alaska. *Arctic and Alpine Research*, *11*(4), 403–420.
694 https://doi.org/10.1080/00040851.1979.12004149

695 Everingham, M., Eslami, S. M. A., Gool, L. V., Williams, C. K. I., Winn, J., & Zisserman, A. (2015). The
696 Pascal Visual Object Classes Challenge: A Retrospective. *International Journal of Computer Vision*,
697 *111*(1), 98–136. https://doi.org/10.1007/s11263-014-0733-5

698 Falaschi, D., Castro, M., Masiokas, M., Tadono, T., & Ahumada, A. L. (2014). Rock Glacier Inventory of
699 the Valles Calchaquíes Region (~ *25*°S), Salta, Argentina, Derived from ALOS Data. Permafrost and
700 Periglacial Processes, 25(1), 69–75. https://doi.org/10.1002/ppp.1801

701 Geiger, S. T., Daniels, J. M., Miller, S. N., & Nicholas, J. W. (2014). Influence of Rock Glaciers on
702 Stream Hydrology in the La Sal Mountains, Utah. *Arctic, Antarctic, and Alpine Research*, *46*(3), *645*–
703 658. https://doi.org/10.1657/1938-4246-46.3.645

704 Haberkorn, A., Kenner, R., Noetzli, J., & Phillips, M. (2021). Changes in ground temperature and
705 dynamics in mountain permafrost in the Swiss Alps. *Frontiers in Earth Science*, *9*.
706 https://doi.org/10.3389/feart.2021.626686

707 Haeberli, W., Hallet, B., Arenson, L., Elconin, R., Humlum, O., Kääb, A., et al. (2006). Permafrost creep
708 and rock glacier dynamics. Permafrost and Periglacial Processes, 17(3), 189–214.
709 https://doi.org/10.1002/ppp.561

710 Hanssen, R. F. (2001). *Radar interferometry : data interpretation and error analysis*. Dordrecht Boston:
711 Kluwer Academic.

712 Harris, S. A., Zhijiu, C., & Guodong, C. (1998). Origin of a bouldery diamiction, Kunlun pass, Qinghai-
713 Xizang Plateau, People's Republic of China: gelifluction deposit or rock glacier? Earth Surface Processes

714 and Landforms, 23(10), 943–952. https://doi.org/10.1002/(sici)1096-9837(199810)23:10<943::aid-
715 esp913>3.0.co;2-7

716 Hassan, J., Chen, X., Muhammad, S., & Bazai, N. A. (2021). Rock glacier inventory, permafrost
717 probability distribution modeling and associated hazards in the Hunza River Basin, Western Karakoram,
718 Pakistan. *Science of the Total Environment*, *782*. https://doi.org/10.1016/j.scitotenv.2021.146833

719 Hu, Y., Liu, L., Wang, X., Zhao, L., Wu, T., Cai, J., et al. (2021). Quantification of permafrost creep
720 provides kinematic evidence for classifying a puzzling periglacial landform. Earth Surface Processes and
721 Landforms, 46(2), 465–477. https://doi.org/10.1002/esp.5039

722 Hu, Y., Liu, L., Huang, L., Zhao, L., & Wu, T. (2021). Rock glacier inventory of the West Kunlun
723 Mountains of China [Dataset]. PANGAEA. https://doi.pangaea.de/10.1594/PANGAEA.938686

724 Huang, L., Liu, L., Jiang, L., & Zhang, T. (2018). Automatic Mapping of Thermokarst Landforms from
725 Remote Sensing Images Using Deep Learning: A Case Study in the Northeastern Tibetan Plateau. *Remote*
726 *Sensing*, *10*(12), 2067. https://doi.org/10.3390/rs10122067

727 Huang, L., Luo, J., Lin, Z., Niu, F., & Liu, L. (2020). Using deep learning to map retrogressive thaw
728 slumps in the Beiluhe region (Tibetan Plateau) from CubeSat images. *Remote Sensing of Environment*,
729 *237*, 111534. https://doi.org/10.1016/j.rse.2019.111534

730 Huang, L., Liu, L., Luo, J., Lin, Z., & Niu, F. (2021). Automatically quantifying evolution of
731 retrogressive thaw slumps in Beiluhe (Tibetan Plateau) from multi-temporal CubeSat images.
732 *International Journal of Applied Earth Observation and Geoinformation*, *102*, 102399.
733 https://doi.org/10.1016/j.jag.2021.102399

734 Huang, L., & Hu, Y. (2023). cryoyan/Landuse_DL: Landuse_DL 2023 (v1.0.0) [Software]. Zenodo.
735 https://doi.org/10.5281/zenodo.7824698

736 Hunter, J. D., 2007. Matplotlib: A 2D graphics environment. *Computing in Science & Engineering*, *9*(3),
737 90–95. https://doi.org/10.1109/mcse.2007.55

738 Ikeda, A., Matsuoka, N., & Kääb, A. (2008). Fast deformation of perennially frozen debris in a warm rock
739 glacier in the Swiss Alps: An effect of liquid water. *Journal of Geophysical Research: Earth Surface*,
740 *113*(1). https://doi.org/10.1029/2007jf000859

741 IPCC (2021). Climate Change 2021: The Physical Science Basis. Contribution of Working Group I to the
742 Sixth Assessment Report of the Intergovernmental Panel on Climate Change In V. Masson-Delmotte, P.
743 Zhai, A. Pirani, S.L. Connors, C. Péan, S. Berger, N. Caud, Y. Chen, L. Goldfarb, M.I. Gomis, M. Huang,
744 K. Leitzell, E. Lonnoy, J.B.R. Matthews, T.K. Maycock, T. Waterfield, O. Yelekçi, R. Yu, and B. Zhou
745 (Ed.)

746 ISCE, 2021. Interferometric Synthetic Aperture Radar Scientific Computing Environment [Software].
747 Retrieved from https://github.com/isce-framework/isce2

748 Janke, J. R. (2007). Colorado Front Range rock glaciers: distribution and topographic characteristics.
749 Arctic, Antarctic, and Alpine Research, 39(1), 74–83.

750 Jones, D. B., Harrison, S., Anderson, K., & Betts, R. A. (2018). Mountain rock glaciers contain globally
751 significant water stores. *Scientific Reports*, *8*(1), 2834. https://doi.org/10.1038/s41598-018-21244-w

752 Jones, D. B., Harrison, S., Anderson, K., Shannon, S., & Betts, R. A. (2021). Rock glaciers represent
753 hidden water stores in the Himalaya. *Science of The Total Environment*, *793*, 145368.
754 https://doi.org/10.1016/j.scitotenv.2021.145368

755 Kenner, R., Pruessner, L., Beutel, J., Limpach, P., & Phillips, M. (2020). How rock glacier hydrology,
756 deformation velocities and ground temperatures interact: Examples from the Swiss Alps. Permafrost and
757 Periglacial Processes, 31(1), 3–14. https://doi.org/10.1002/ppp.2023

758 Kofler, C., Mair, V., Comiti, F., Zebisch, M., Schneiderbauer, S., & Steger, S. (2022). Towards a
759 sediment transfer capacity index of rock glaciers: Examples from two catchments in South Tyrol, (Eastern
760 Italian Alps). *Catena*, *216*, 106329. https://doi.org/10.1016/j.catena.2022.106329

761 Kummert, M., & Delaloye, R. (2018). Mapping and quantifying sediment transfer between the front of
762 rapidly moving rock glaciers and torrential gullies. Geomorphology, *309*, 60–76.
763 https://doi.org/10.1016/j.geomorph.2018.02.021

764 LeCun, Y., Bengio, Y., & Hinton, G. (2015). Deep learning. Nature, *521*(7553), 436–444.
765 https://doi.org/10.1038/nature14539

766 Li, J. (1986). *Tibetan glaciers*. Beijing: Science Press.

767 Li, K., Chen, J., Zhao, L., Zhang, X., Pang, Q., Fang, H., & Liu, G. (20*12*). Permafrost distribution in
768 typical area of West Kunlun Mountains derived from a comprehensive survey. *Journal of Glaciology and*
769 *Geocryology*, *34*(2), 447–454.

770 Liu, L., Millar, C. I., Westfall, R. D., & Zebker, H. A. (2013). Surface motion of active rock glaciers in
771 the Sierra Nevada, California, USA: Inventory and a case study using InSAR. Cryosphere, 7(4), *11*09–
772 1119. https://doi.org/10.5194/tc-7-1109-2013

773 Marcer, M., Cicoira, A., Cusicanqui, D., Bodin, X., Echelard, T., Obregon, R., & Schoeneich, P. (2021).
774 Rock glaciers throughout the French Alps accelerated and destabilised since 1990 as air temperatures
775 increased. *Communications Earth and Environment*, *2*(1), 81. https://doi.org/10.1038/s43247-021-00150-
776 6

777 Marcer, Marco. (2020). Rock glaciers automatic mapping using optical imagery and convolutional neural
778 networks. Permafrost and Periglacial Processes, 31(4), 561–566. https://doi.org/10.1002/ppp.2076

779 Millar, C.I., & Westfall, R. D. (2008). Rock glaciers and related periglacial landforms in the Sierra
780 Nevada, CA, USA; inventory, distribution and climatic relationships. *Quaternary International*, *188*(1),
781 90–104. https://doi.org/10.1016/j.quaint.2007.06.004

782 Millar, Constance I., Westfall, R. D., & Delany, D. L. (2013). Thermal and hydrologic attributes of rock
783 glaciers and periglacial talus landforms: Sierra Nevada, California, USA. Quaternary International, *310*,
784 169–180. https://doi.org/10.1016/j.quaint.2012.07.019

785 Mottaghi, R., Chen, X., Liu, X., Cho, N.-G., Lee, S.-W., Fidler, S., et al. (2014). The role of context for
786 object detection and semantic segmentation in the wild. In *Computer Vision and Pattern Recognition* (pp.
787 891–898). Columbus, OH.

788 Müller, J., Vieli, A., & Gärtner-Roer, I. (2016). Rock glaciers on the run - Understanding rock glacier
789 landform evolution and recent changes from numerical flow modeling. Cryosphere, 10(6), 2865–2886.
790 https://doi.org/10.5194/tc-10-2865-2016

791 Ni, J., Wu, T., Zhu, X., Hu, G., Zou, D., Wu, X., et al. (2021). Simulation of the Present and Future
792 Projection of Permafrost on the Qinghai-Tibet Plateau with Statistical and Machine Learning Models.
793 *Journal of Geophysical Research: Atmospheres*, *126*(2). https://doi.org/10.1029/2020jd033402

794 Obu, J., Westermann, S., Bartsch, A., Berdnikov, N., Christiansen, H. H., Dashtseren, A., et al. (2019).
795 Northern Hemisphere permafrost map based on TTOP modelling for 2000–2016 at 1 km2 scale. *Earth-*
796 *Science Reviews*, *193*, 299–316. https://doi.org/10.1016/j.earscirev.2019.04.023

797 Onaca, A., Ardelean, F., Urdea, P., & Magori, B. (2017). Southern Carpathian rock glaciers: Inventory,
798 distribution and environmental controlling factors. Geomorphology, 293, 391–404.
799 https://doi.org/10.1016/j.geomorph.2016.03.032

800 Peel, M. C., Finlayson, B. L., & McMahon, T. A. (2007). Updated world map of the Köppen-Geiger
801 climate classification. *Hydrology and Earth System Sciences*, *11*(5), 1633–1644.
802 https://doi.org/10.5194/hess-11-1633-2007

803 QGIS Development Team, 2009. QGIS Geographic Information System [Software]. Retrieved from
804 http://qgis.osgeo.org

805 Ran, Z., & Liu, G. (2018). Rock glaciers in Daxue Shan, south-eastern Tibetan Plateau: an inventory,
806 their distribution, and their environmental controls. The Cryosphere, 12(7), 2327–2340.
807 https://doi.org/10.5194/tc-12-2327-2018

808 Ran, Y., Li, X., Cheng, G., Nan, Z., Che, J., Sheng, Y., et al. (2021). Mapping the permafrost stability on
809 the Tibetan Plateau for 2005–2015. *Science China Earth Sciences*, *64*(1), 62–79.
810 https://doi.org/10.1007/s11430-020-9685-3

811 Rangecroft, S., Harrison, S., Anderson, K., Magrath, J., Castel, A. P., & Pacheco, P. (2014). A First Rock
812 Glacier Inventory for the Bolivian Andes. Permafrost and Periglacial Processes, 25(4), 333–343.
813 https://doi.org/10.1002/ppp.1816

814 Reinosch, E., Gerke, M., Riedel, B., Schwalb, A., Ye, Q., & Buckel, J. (2021). Rock glacier inventory of
815 the western Nyainqêntanglha Range, Tibetan Plateau, supported by InSAR time series and automated
816 classification. Permafrost and Periglacial Processes, 32(4), 657–672. https://doi.org/10.1002/ppp.2117

817 RGIK. (2022a). *Towards standard guidelines for inventorying rock glaciers: baseline concepts (Version*
818 *4.2.2)* (p. 13).

819 RGIK. (2022b). *Towards standard guidelines for inventorying rock glaciers: practical concepts (Version*
820 *2.0))* (p. 10).

821 Robson, B. A., Bolch, T., MacDonell, S., Hölbling, D., Rastner, P., & Schaffer, N. (2020). Automated
822 detection of rock glaciers using deep learning and object-based image analysis. Remote Sensing of
823 Environment, *250*, 112033. https://doi.org/10.1016/j.rse.2020.112033

824 Roer, I., & Nyenhuis, M. (2007). Rockglacier activity studies on a regional scale: comparison of
825 geomorphological mapping and photogrammetric monitoring. Earth Surface Processes and Landforms,
826 32(12), 1747–1758. https://doi.org/10.1002/esp.1496

827 Sakai, A. (2019). Brief communication: Updated GAMDAM glacier inventory over high-mountain Asia.
828 *The Cryosphere*, *13*(7), 2043–2049. https://doi.org/10.5194/tc-13-2043-2019

829 Schaffer, N., MacDonell, S., Réveillet, M., Yáñez, E., & Valois, R. (2019). Rock glaciers as a water
830 resource in a changing climate in the semiarid Chilean Andes. *Regional Environmental Change*, *19*(5),
831 1263–1279. https://doi.org/10.1007/s10113-018-01459-3

832 Schmid, M.-O., Baral, P., Gruber, S., Shahi, S., Shrestha, T., Stumm, D., & Wester, P. (2015).
833 Assessment of permafrost distribution maps in the Hindu Kush Himalayan region using rock glaciers
834 mapped in Google Earth. The Cryosphere, 9(6), 2089–2099. https://doi.org/10.5194/tc-9-2089-2015

835 Scotti, R., Brardinoni, F., Alberti, S., Frattini, P., & Crosta, G. B. (2013). A regional inventory of rock
836 glaciers and protalus ramparts in the central Italian Alps. Geomorphology, *186*, 136–149.
837 https://doi.org/10.1016/j.geomorph.2012.12.028

838 Sorg, A., Kääb, A., Roesch, A., Bigler, C., & Stoffel, M. (2015). Contrasting responses of Central Asian
839 rock glaciers to global warming. Scientific Reports, 5(1), 8228. https://doi.org/10.1038/srep08228

840 Thibert, E., & Bodin, X. (2022). Changes in surface velocities over four decades on the Laurichard rock
841 glacier (French Alps). Permafrost and Periglacial Processes, 33(3), 323–335.
842 https://doi.org/10.1002/ppp.2159

843 Villarroel, C. D., Beliveau, G. T., Forte, A. P., Monserrat, O., & Morvillo, M. (2018). DInSAR for a
844 regional inventory of active rock glaciers in the Dry Andes Mountains of Argentina and Chile with
845 sentinel-1 data. Remote Sensing, 10(10), 1588. https://doi.org/10.3390/rs10101588

846 Wang, X., Liu, L., Zhao, L., Wu, T., Li, Z., & Liu, G. (2017). Mapping and inventorying active rock
847 glaciers in the northern Tien Shan of China using satellite SAR interferometry. Cryosphere, 11(2), 997–
848 1014. https://doi.org/10.5194/tc-11-997-2017

849 Wirz, V., Gruber, S., Purves, R. S., Beutel, J., Gärtner-Roer, I., Gubler, S., & Vieli, A. (2016). Short-term
850 velocity variations at three rock glaciers and their relationship with meteorological conditions. *Earth*
851 *Surface Dynamics*, *4*(1), 103–123. https://doi.org/10.5194/esurf-4-103-2016

852 Yang, M., Nelson, F. E., Shiklomanov, N. I., Guo, D., & Wan, G. (2010). Permafrost degradation and its
853 environmental effects on the Tibetan Plateau: A review of recent research. *Earth-Science Reviews*, *103*(1–
854 2), 31–44. https://doi.org/10.1016/j.earscirev.2010.07.002

855 Yang, M., Wang, X., Pang, G., Wan, G., & Liu, Z. (2019). The Tibetan Plateau cryosphere: Observations
856 and model simulations for current status and recent changes. Earth-Science Reviews, *190*, 353–369.
857 https://doi.org/10.1016/j.earscirev.2018.12.018

858 Yao, T., Xue, Y., Chen, D., Chen, F., Thompson, L., Cui, P., et al. (2018). Recent Third Pole's rapid
859 warming accompanies cryospheric melt and water cycle intensification and interactions between monsoon
860 and environment: multi-disciplinary approach with observation, modeling and analysis Recent Third
861 Pole's rapid warming accompanies cryospheric melt and water cycle intensification and interactions
862 between monsoon and environment: multi-disciplinary approach with observation, modeling and analysis.

Bulletin of the American Meteorological Society, *100*(3), 423–444. https://doi.org/10.1175/bams-d-17-0057.1

Zhang, E., Liu, L., Huang, L., & Ng, K. S. (2021). An automated, generalized, deep-learning-based method for delineating the calving fronts of Greenland glaciers from multi-sensor remote sensing imagery. Remote Sensing of Environment, *254*, 112265. https://doi.org/10.1016/j.rse.2020.112265

Zhang, G., Yao, T., Xie, H., Yang, K., Zhu, L., Shum, C. K., et al. (2020). Response of Tibetan Plateau lakes to climate change: Trends, patterns, and mechanisms. Earth-Science Reviews, *208*, 103269. https://doi.org/10.1016/j.earscirev.2020.103269

Zhang, X., Feng, M., Zhang, H., Wang, C., Tang, Y., Xu, J., et al. (2021). Detecting rock glacier displacement in the central himalayas using multi-temporal insar. Remote Sensing, 13(23), 4738. https://doi.org/10.3390/rs13234738

Zhang, Q., Jia, N., Xu, H., Yi, C., Wang, N., & Zhang, L. (2022). Rock glaciers in the Gangdise Mountains, southern Tibetan Plateau: Morphology and controlling factors. *CATENA*, *218*, 106561. https://doi.org/10.1016/j.catena.2022.106561

Zhao, L., & Sheng, Y. (2019). *Permafrost in the Qinghai-Tibet plateau and its changes*. Beijing: Science Press.

Zhao, L., Zou, D., Hu, G., Du, E., Pang, Q., Xiao, Y., et al. (2020). Changing climate and the permafrost environment on the Qinghai–Tibet (Xizang) plateau. Permafrost and Periglacial Processes, 31(3), 396–405. https://doi.org/10.1002/ppp.2056

Zhao, L., Zou, D., Hu, G., Wu, T., Du, E., Liu, G., et al. (2021). A synthesis dataset of permafrost thermal state for the Qinghai–Tibet (Xizang) Plateau, China. *Earth System Science Data*, *13*(8), 4207–4218. https://doi.org/10.5194/essd-13-4207-2021

Zhu, C., Zhang, J., & Cheng, P. (1996). Rock glaciers in the Central Tianshan Mountains, China. Permafrost and Periglacial Processes, 7(1), 69–78. https://doi.org/10.1002/(sici)1099-1530(199601)7:1<69::aid-ppp210>3.0.co;2-b

Zou, D., Zhao, L., Sheng, Y., Chen, J., Hu, G., Wu, T., et al. (2017). A new map of permafrost distribution on the Tibetan Plateau. The Cryosphere, 11(6), 2527–2542. https://doi.org/10.5194/tc-11-2527-2017

Figure 1.

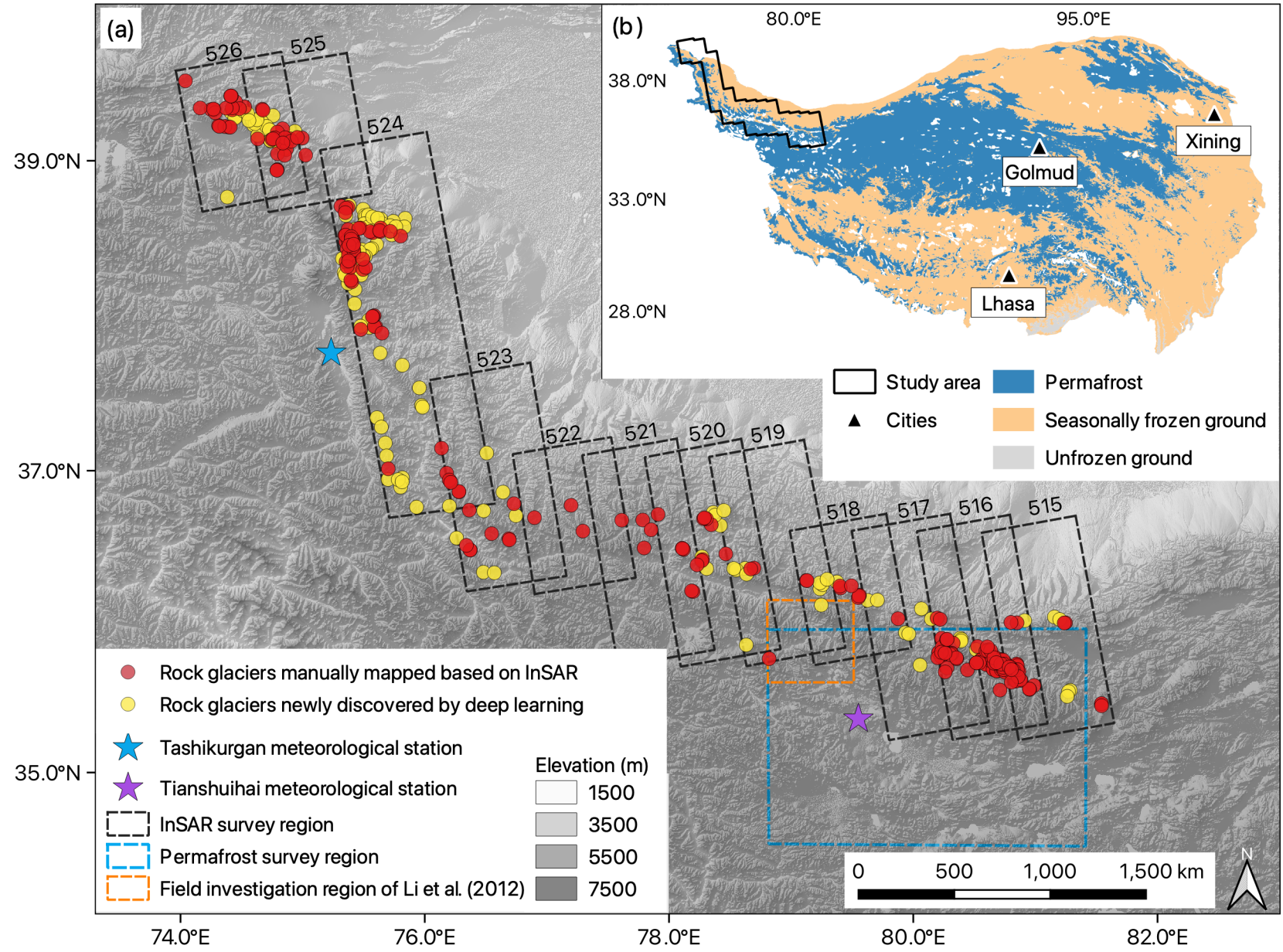
(a)
526
525
524
523
522
521
520
519
518
517
516
515
39.0°N
37.0°N
35.0°N
74.0°E
76.0°E
78.0°E
80.0°E
82.0°E
(b)
80.0°E
95.0°E
38.0°N
33.0°N
28.0°N
Xining
Golmud
Lhasa
Study area
Cities
Permafrost
Seasonally frozen ground
Unfrozen ground
Rock glaciers manually mapped based on InSAR
Rock glaciers newly discovered by deep learning
Tashikurgan meteorological station
Tianshuihai meteorological station
InSAR survey region
Permafrost survey region
Field investigation region of Li et al. (2012)
Elevation (m)
1500
3500
5500
7500
0
500
1,000
1,500 km
N

Figure 2.

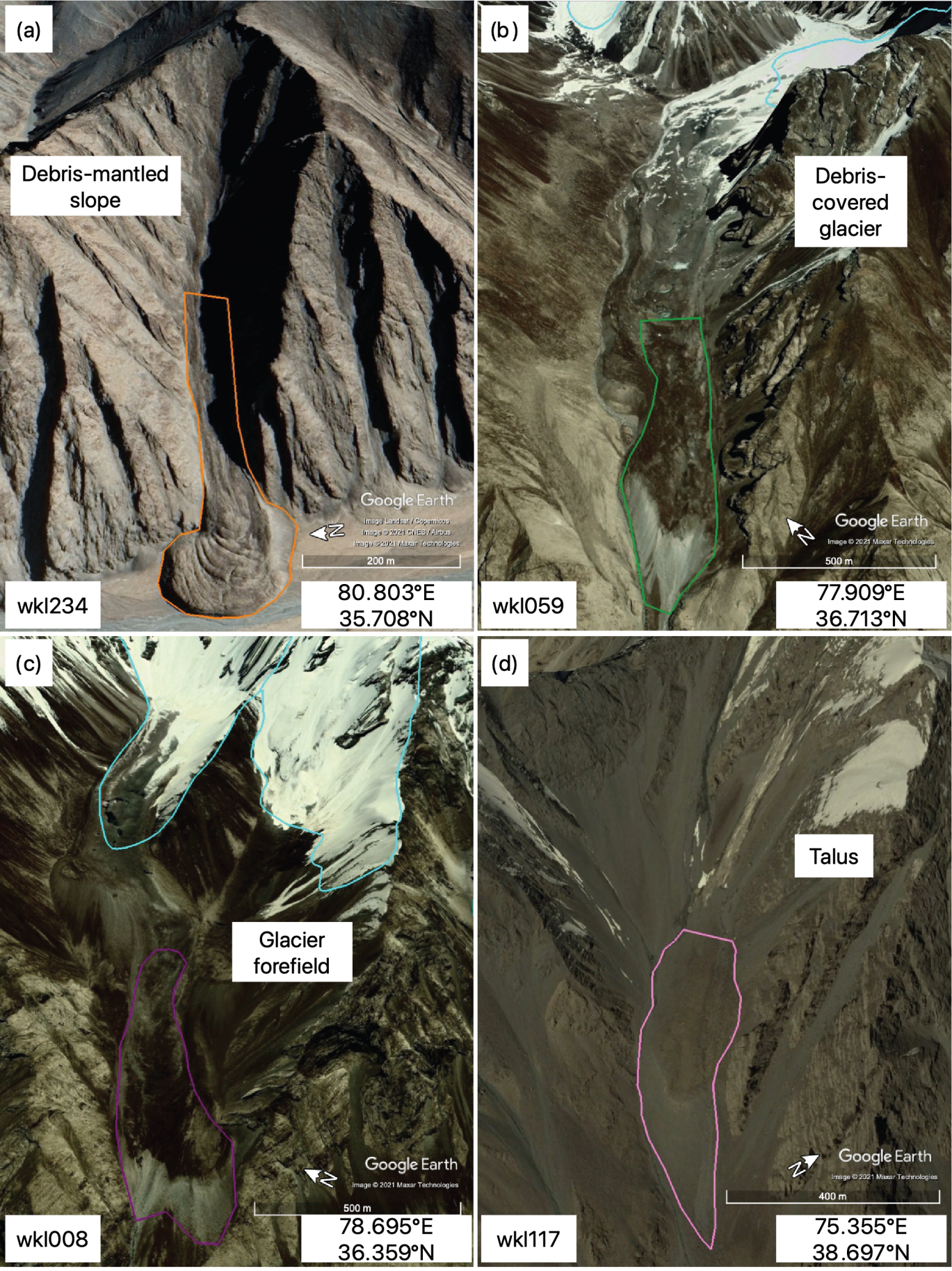

Debris-mantled slope-connected rock glaciers (DMS-RGs)

Glacier-connected rock glaciers (G-RGs)

Glacier forefield-connected rock glaciers (GF-RGs)

Talus-connected rock glaciers (T-RGs)

Glacier outlined by GLIMS

Figure 3.

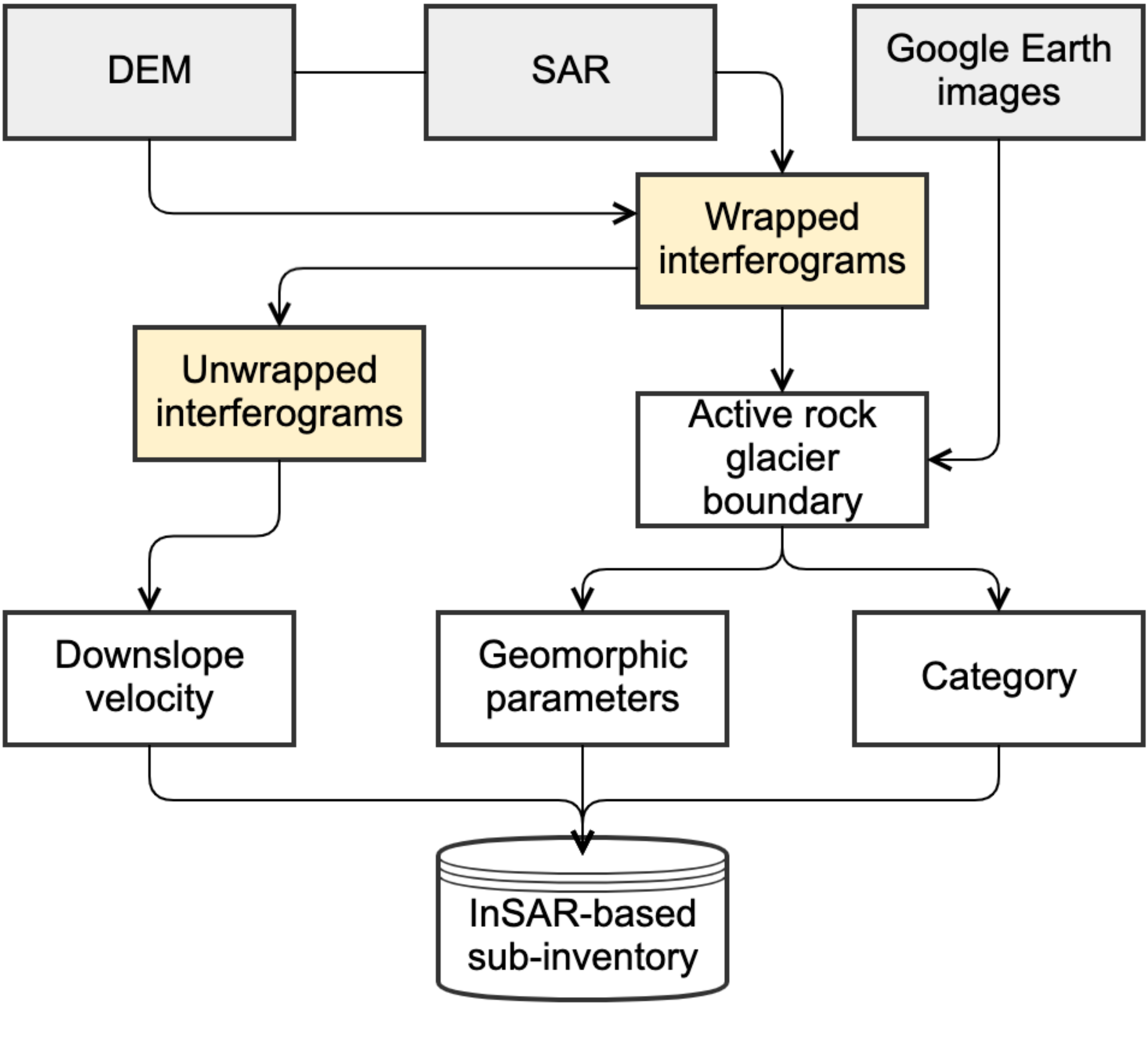
DEM
SAR
Google Earth images
Wrapped interferograms
Unwrapped interferograms
Active rock glacier boundary
Downslope velocity
Geomorphic parameters
Category
InSAR-based sub-inventory

Figure 4.

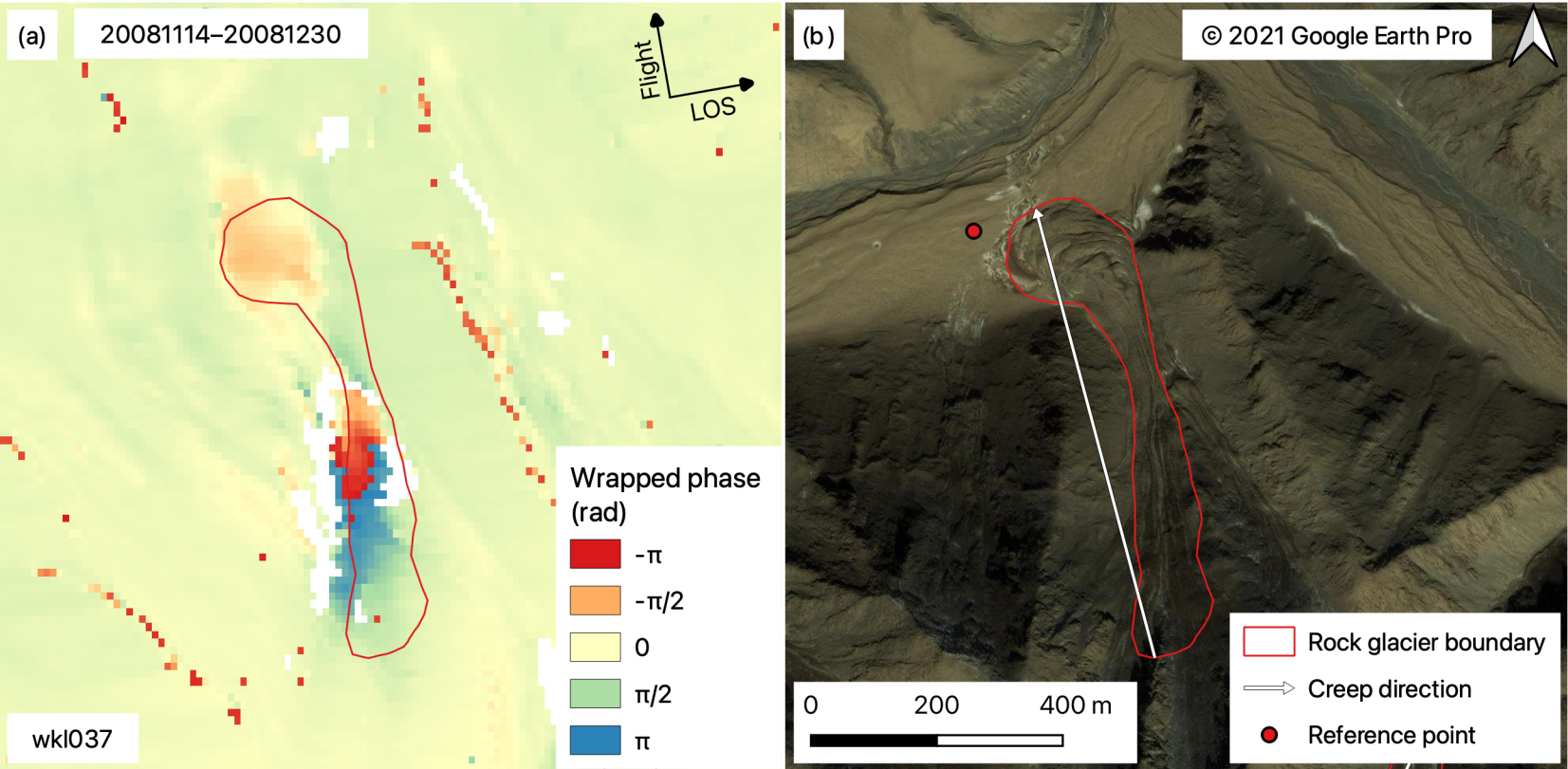
(a)
20081114–20081230
Flight
LOS
Wrapped phase (rad)
-π
-π/2
0
π/2
π
wkl037
(b)
© 2021 Google Earth Pro
0
200
400 m
Rock glacier boundary
Creep direction
Reference point

Figure 5.

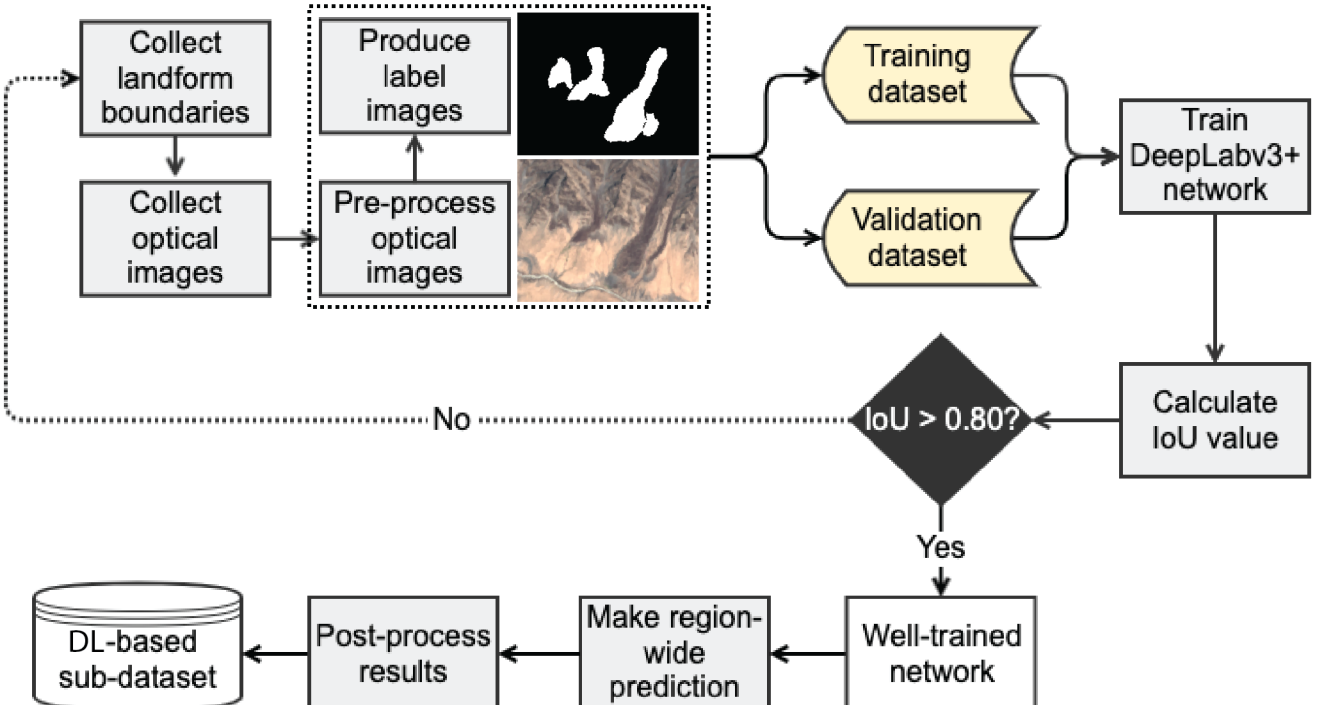
Collect landform boundaries
Collect optical images
Pre-process optical images
Produce label images
Training dataset
Validation dataset
Train DeepLabv3+ network
Calculate IoU value
IoU > 0.80?
No
Yes
Well-trained network
Make region-wide prediction
Post-process results
DL-based sub-dataset

Figure 6.

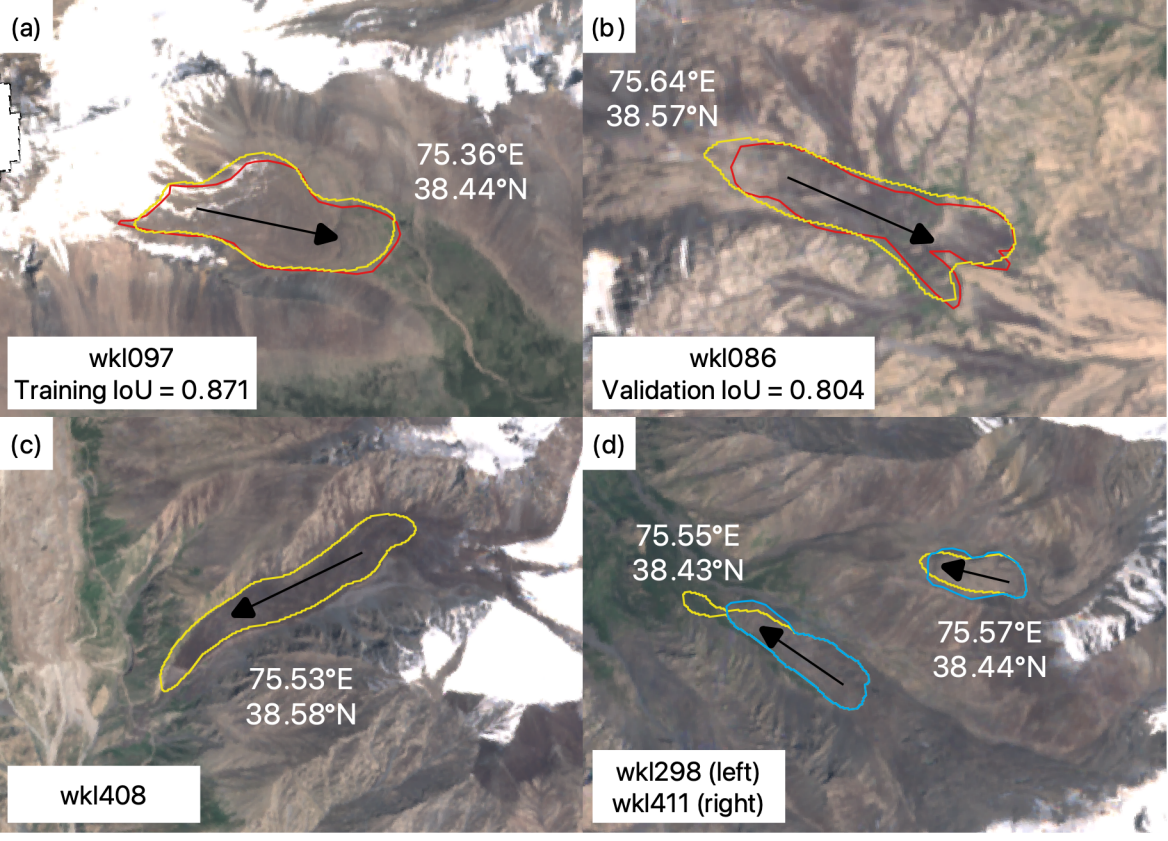
(a)
75.36°E
38.44°N
wkl097
Training IoU = 0.871
(b)
75.64°E
38.57°N
wkl086
Validation IoU = 0.804
(c)
75.53°E
38.58°N
wkl408
(d)
75.55°E
38.43°N
75.57°E
38.44°N
wkl298 (left)
wkl411 (right)
Deep learning delineated boundary
Manually delineated boundary in the InSAR-based inventory
Manually modified boundary after automated mapped outline
0
500
1,000 m

Figure 7.

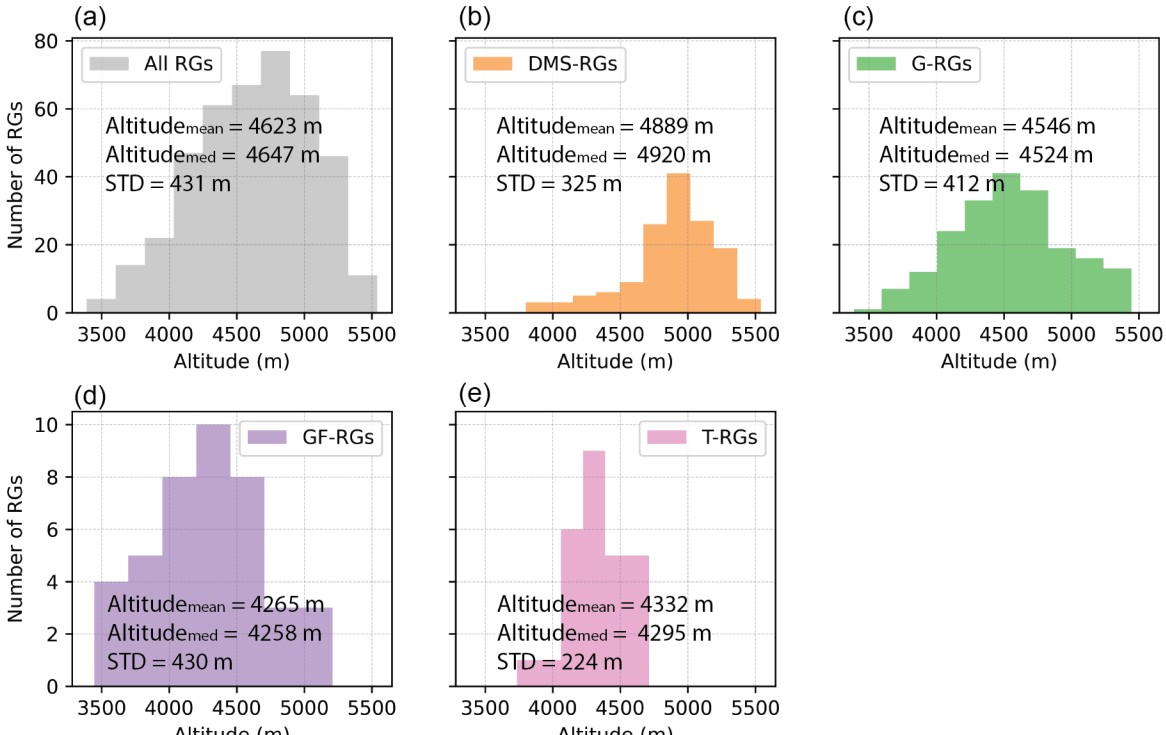
(a)
All RGs
Altitude$_{mean}$ = 4623 m
Altitude$_{med}$ = 4647 m
STD = 431 m
Number of RGs
Altitude (m)
(b)
DMS-RGs
Altitude$_{mean}$ = 4889 m
Altitude$_{med}$ = 4920 m
STD = 325 m
Altitude (m)
(c)
G-RGs
Altitude$_{mean}$ = 4546 m
Altitude$_{med}$ = 4524 m
STD = 412 m
Altitude (m)
(d)
GF-RGs
Altitude$_{mean}$ = 4265 m
Altitude$_{med}$ = 4258 m
STD = 430 m
Number of RGs
Altitude (m)
(e)
T-RGs
Altitude$_{mean}$ = 4332 m
Altitude$_{med}$ = 4295 m
STD = 224 m
Altitude (m)

Figure 8.

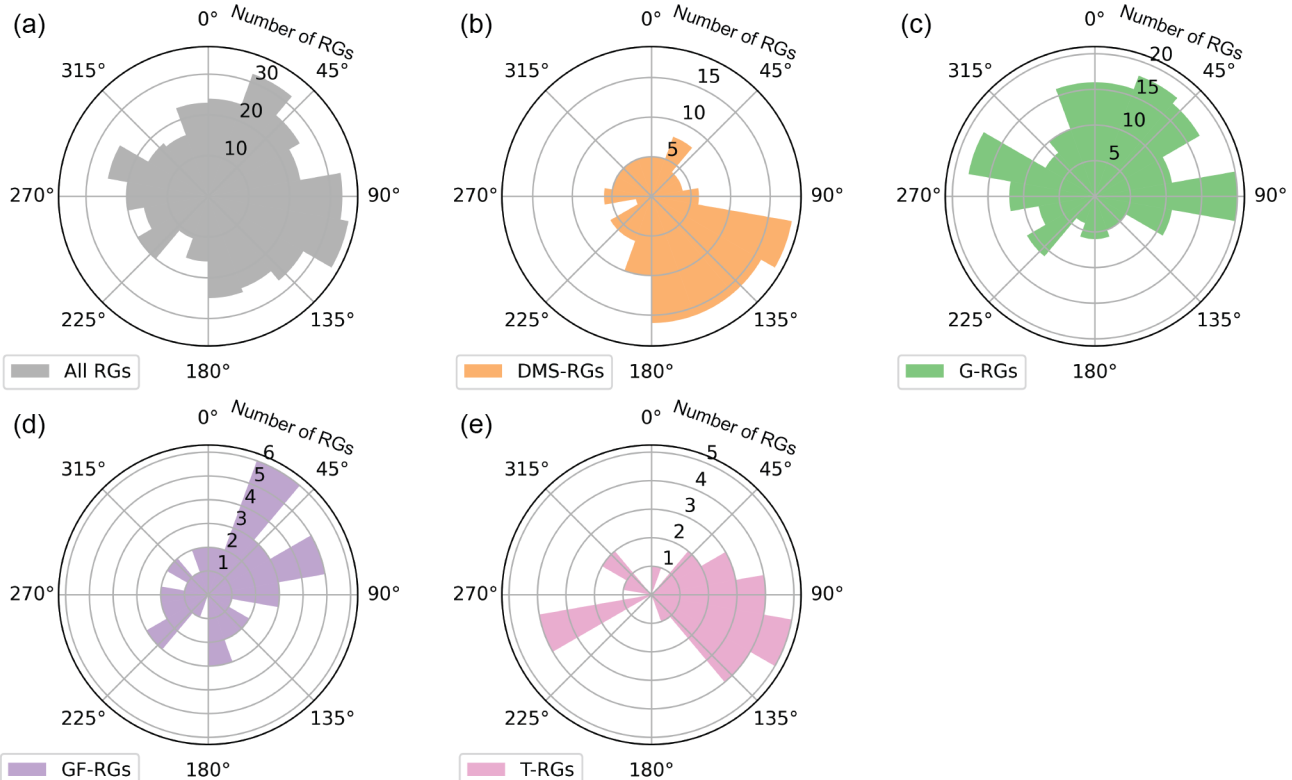
(a)
0°
Number of RGs
45°
90°
135°
180°
225°
270°
315°
10
20
30
All RGs
(b)
5
10
15
DMS-RGs
(c)
5
10
15
20
G-RGs
(d)
1
2
3
4
5
6
GF-RGs
(e)
1
2
3
4
5
T-RGs

Figure 9.

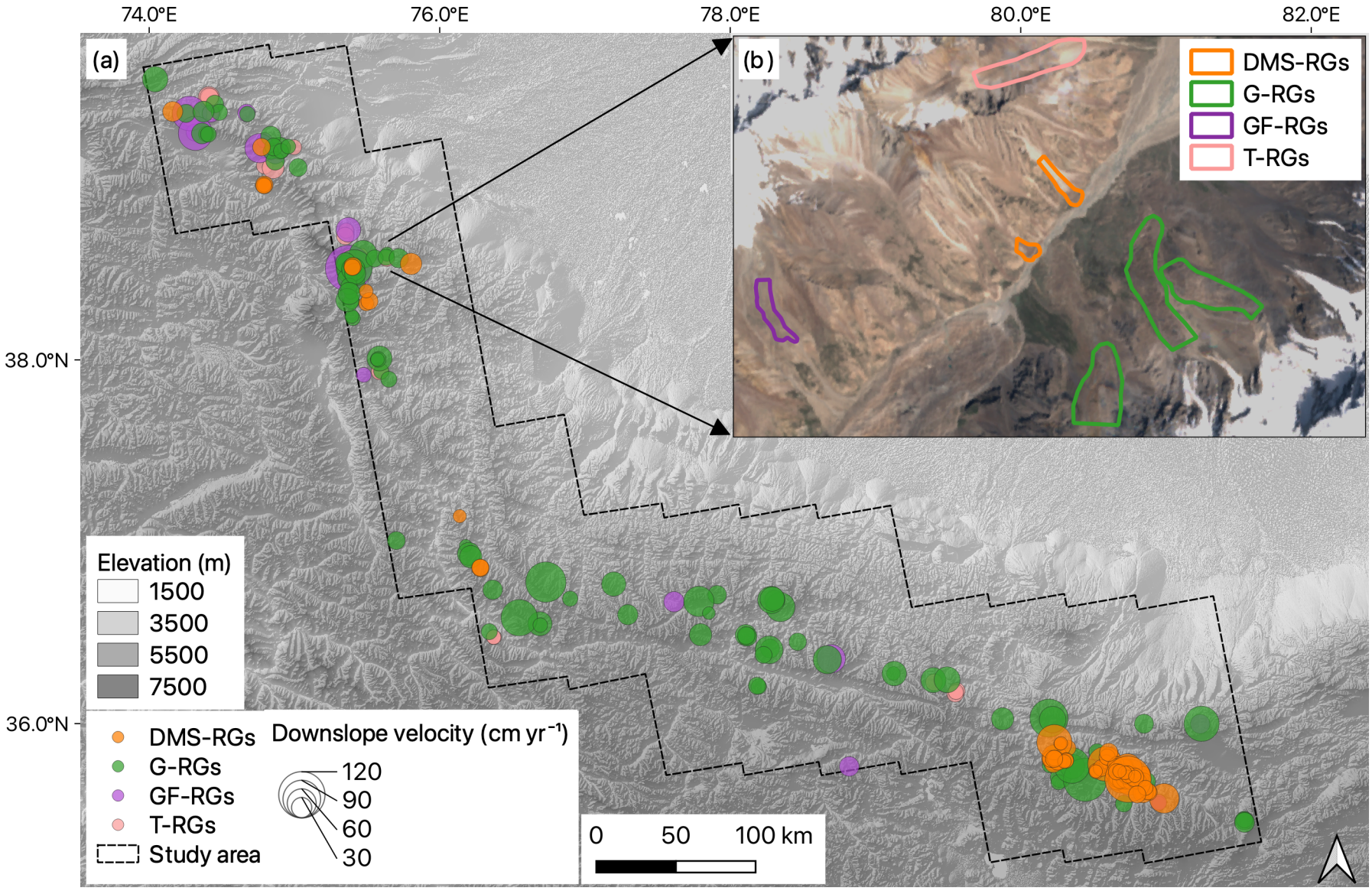
74.0°E
76.0°E
78.0°E
80.0°E
82.0°E
38.0°N
36.0°N
(a)
(b)
DMS-RGs
G-RGs
GF-RGs
T-RGs
Elevation (m)
1500
3500
5500
7500
DMS-RGs
G-RGs
GF-RGs
T-RGs
Study area
Downslope velocity (cm yr⁻¹)
120
90
60
30
0
50
100 km

Figure 10.

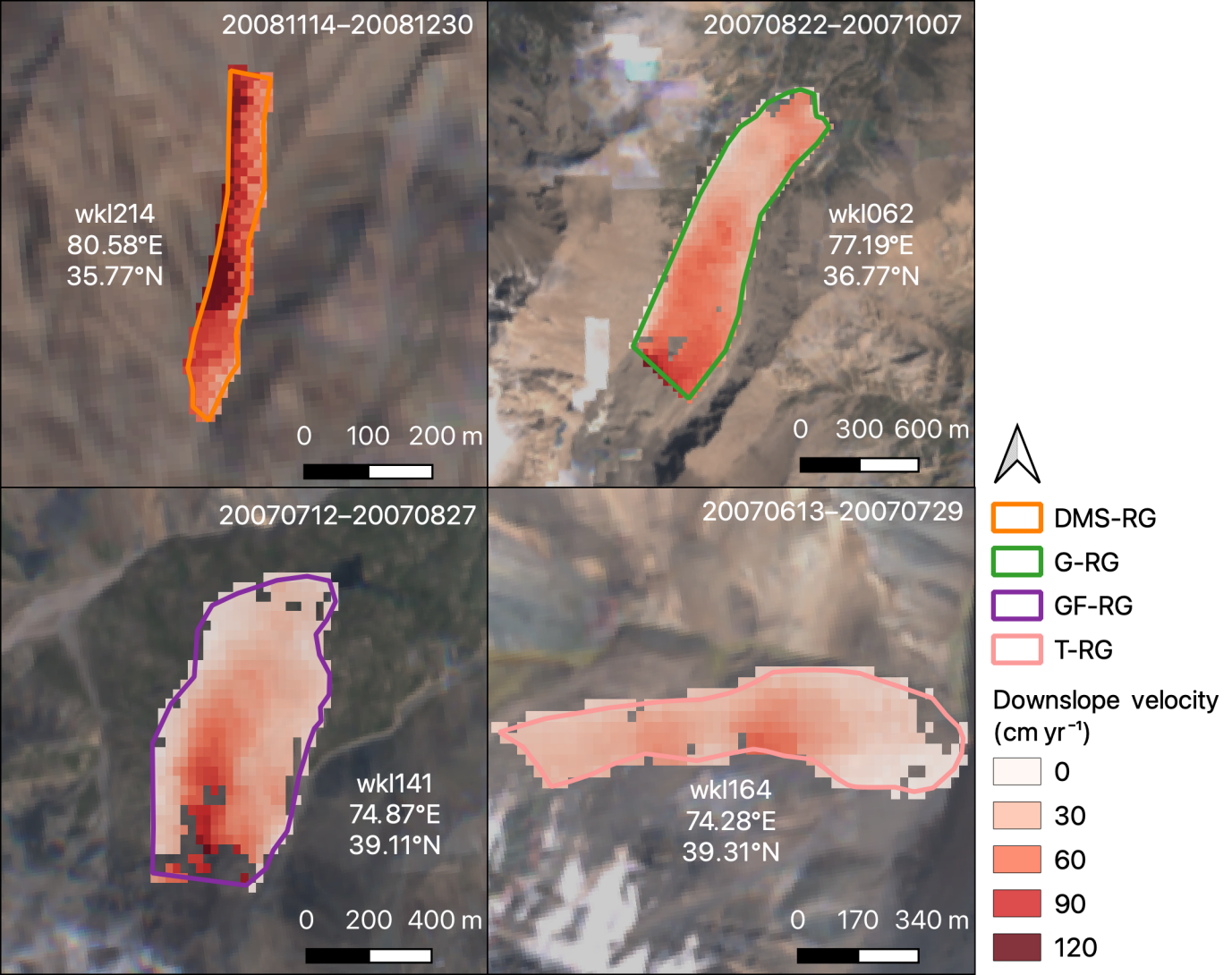
20081114–20081230
wkl214
80.58°E
35.77°N
0 100 200 m
20070822–20071007
wkl062
77.19°E
36.77°N
0 300 600 m
20070712–20070827
wkl141
74.87°E
39.11°N
0 200 400 m
20070613–20070729
wkl164
74.28°E
39.31°N
0 170 340 m
DMS-RG
G-RG
GF-RG
T-RG
Downslope velocity (cm yr⁻¹)
0
30
60
90
120

Figure 11.

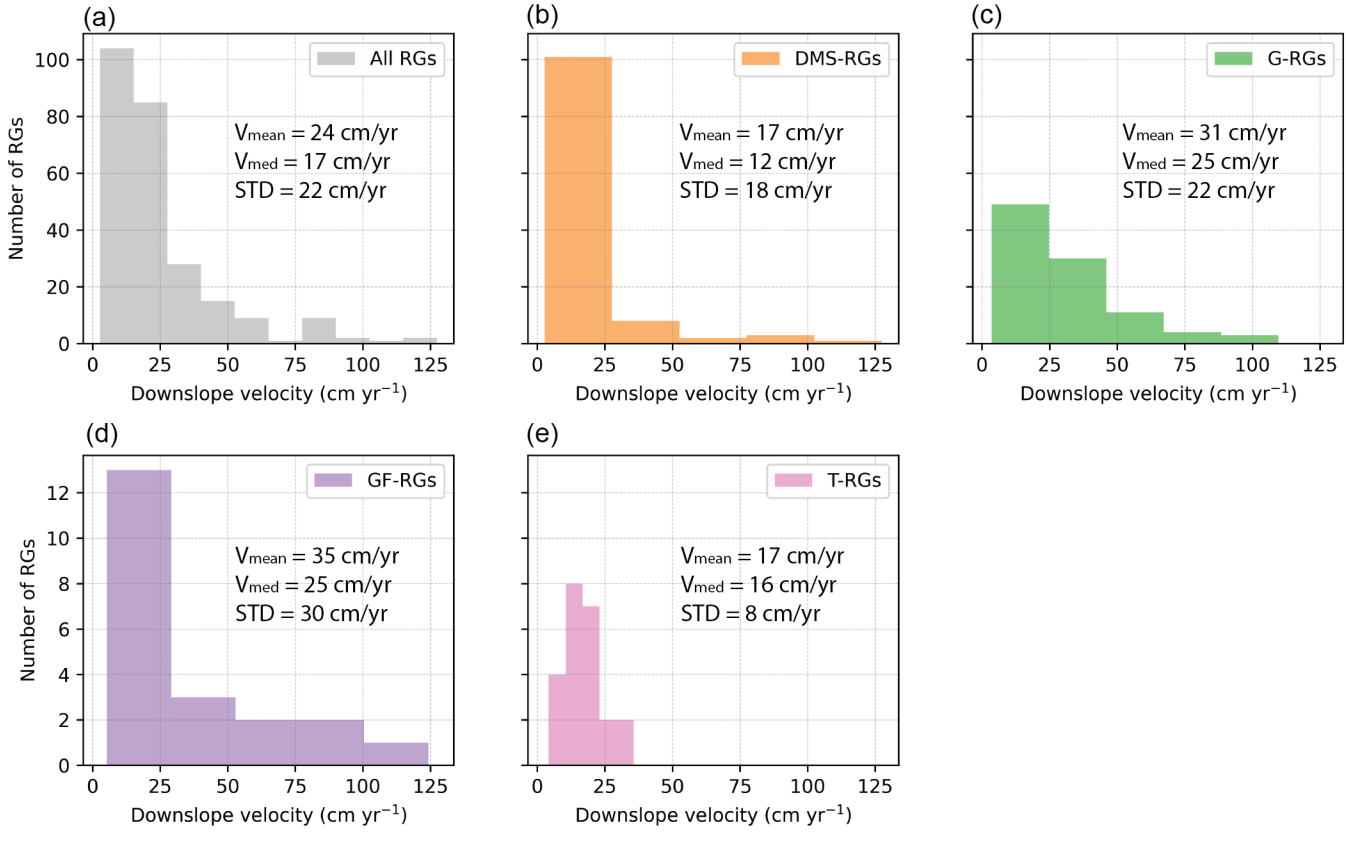
(a)
All RGs
V_{mean} = 24 cm/yr
V_{med} = 17 cm/yr
STD = 22 cm/yr
Number of RGs
Downslope velocity (cm yr^{-1})
(b)
DMS-RGs
V_{mean} = 17 cm/yr
V_{med} = 12 cm/yr
STD = 18 cm/yr
Downslope velocity (cm yr^{-1})
(c)
G-RGs
V_{mean} = 31 cm/yr
V_{med} = 25 cm/yr
STD = 22 cm/yr
Downslope velocity (cm yr^{-1})
(d)
GF-RGs
V_{mean} = 35 cm/yr
V_{med} = 25 cm/yr
STD = 30 cm/yr
Number of RGs
Downslope velocity (cm yr^{-1})
(e)
T-RGs
V_{mean} = 17 cm/yr
V_{med} = 16 cm/yr
STD = 8 cm/yr
Downslope velocity (cm yr^{-1})

Figure 12.

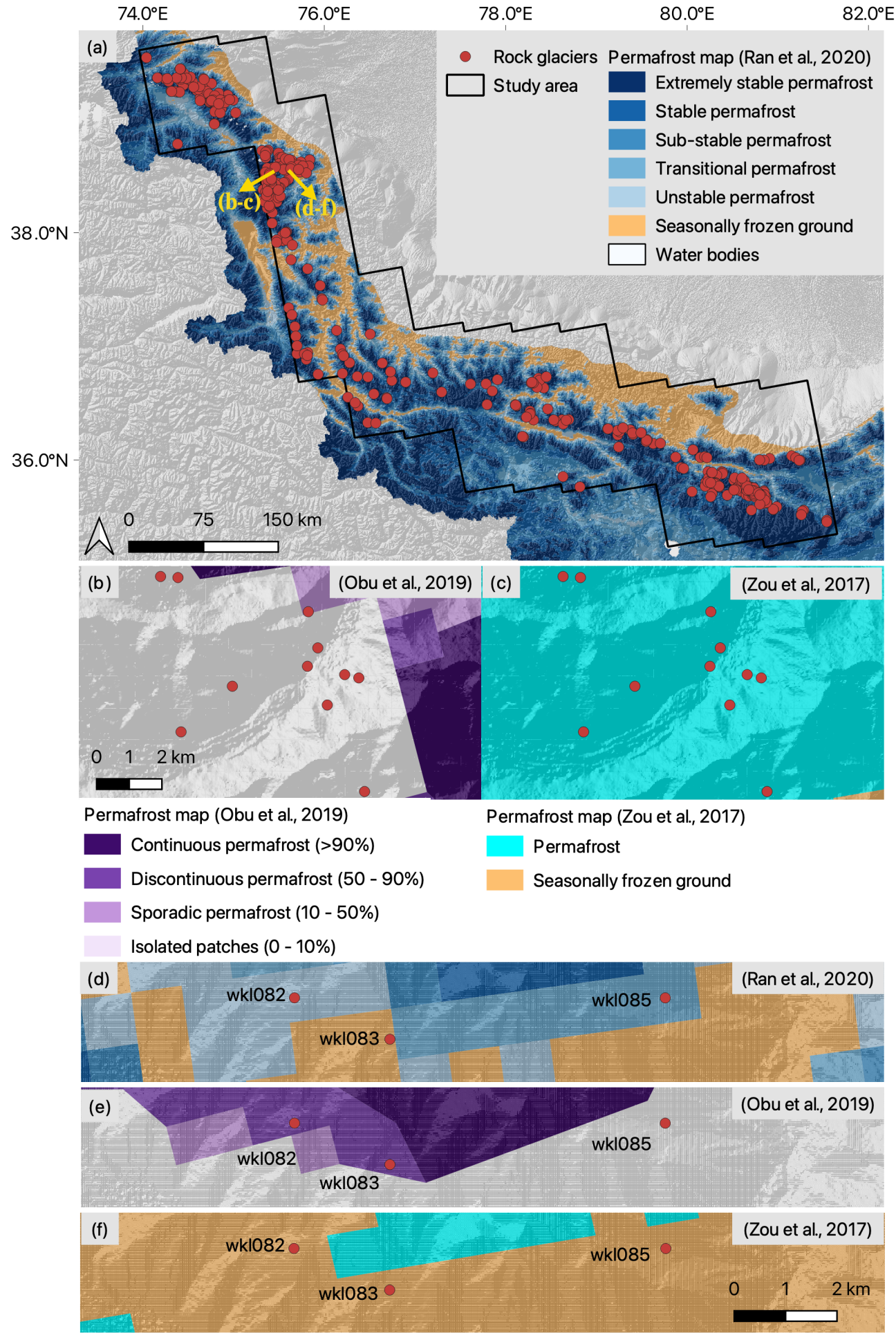
74.0°E
76.0°E
78.0°E
80.0°E
82.0°E
38.0°N
36.0°N
(a)
Rock glaciers
Study area
Permafrost map (Ran et al., 2020)
Extremely stable permafrost
Stable permafrost
Sub-stable permafrost
Transitional permafrost
Unstable permafrost
Seasonally frozen ground
Water bodies
(b-c)
(d-f)
0 75 150 km
(b)
(Obu et al., 2019)
0 1 2 km
(c)
(Zou et al., 2017)
Permafrost map (Obu et al., 2019)
Continuous permafrost (>90%)
Discontinuous permafrost (50 - 90%)
Sporadic permafrost (10 - 50%)
Isolated patches (0 - 10%)
Permafrost map (Zou et al., 2017)
Permafrost
Seasonally frozen ground
(d)
(Ran et al., 2020)
wkl082
wkl083
wkl085
(e)
(Obu et al., 2019)
wkl082
wkl083
wkl085
(f)
(Zou et al., 2017)
wkl082
wkl083
wkl085
0 1 2 km